CT image-based estimation of permeability evolution of wellbore cement under geologic carbon sequestration conditions

Xiuxiu Miao[1], Manguang Gan[2], Yan Wang[2], Liwei Zhang[2], and Hongwen Jing[1]

[1]China University of Mining and Technology
[2]Institute of Rock and Soil Mechanics

November 21, 2022

Abstract

The combination of X-ray imaging and CT image-based computational fluid dynamics (CFD) simulation allows study of flow in fractured porous media. In this study, X-ray imaging was employed to unveil the morphological and aperture alterations of artificial fractures in wellbore cement cores that were exposed to CO2-saturated brine under geologic carbon sequestration (GCS) conditions. Direct pore-scale modelling of fluid flow through 3D fractures reconstructed from CT images was carried out to reveal velocity distribution in the fracture and for estimation of local and average permeability of the fracture. Varying-radius pipe representations of the fractures were established using the optimal characteristic radius formulation that was determined from the relation of flow cross-section shape and conductivity based on direct pore-scale modelling. Varying-radius pipeline modelling of fluid flow through simplified fractures was also implemented and the local and average permeability results based on varying-radius pipeline modelling were compared against those based on direct pore-scale modelling. The fracture after CO2 exposure in the reactive diffusion process was covered by substantial precipitated calcite, and the permeability of the fracture decreased from 4.15×10-8 m2 to 2.96×10-8 m2. In contrast, the fracture after CO2 exposure in the reactive flow process underwent significant dissolution, a large number of tensile micro-fractures were formed at the surface of the fracture, and the permeability of the fracture increased from 3.91×10-8 m2 to 4.23×10-8 m2. The relative error of the average fracture permeability obtained from direct pore-scale modelling (-7.33%-4.05%) was comparable with that obtained from varying-radius pipeline modelling (-7.77%-10.64%).

CT image–based estimation of permeability evolution of wellbore cement under geologic carbon sequestration conditions

Xiuxiu Miao[1]; michelle.xiuxiu.miao@gmail.com

Manguang Gan[2,3]; cumtgmg@163.com

Yan Wang[2]; ywang@whrsm.ac.cn

Liwei Zhang[2,3*]; lwzhang@whrsm.ac.cn

Hongwen Jing[1*]; hwjingcumt@126.com

1. *State Key Laboratory for Geomechanics and Deep Underground Engineering, China University of Mining and Technology, Xuzhou, Jiangsu Province 221116, China*
2. *State Key Laboratory of Geo-mechanics and Geo-technical Engineering, Institute of Rock and Soil Mechanics, Chinese Academy of Sciences, Wuhan, Hubei Province, 430071, China*
3. *University of Chinese Academy of Sciences, Beijing, 100049, China*

Abstract

The combination of X-ray imaging and CT image–based computational fluid dynamics (CFD) simulation allows study of flow in fractured porous media. In this study, X-ray imaging was employed to unveil the morphological and aperture alterations of artificial fractures in wellbore cement cores that were exposed to CO_2-saturated brine under geologic carbon sequestration (GCS) conditions. Direct pore-scale modelling of fluid flow through 3D fractures reconstructed from CT images was carried out to reveal velocity distribution in the fracture and for estimation of local and average permeability of the fracture. Varying-radius pipe representations of the fractures were established using the optimal characteristic radius formulation that was determined from the relation of flow cross-section shape and conductivity based on direct pore-scale modelling. Varying-radius pipeline modelling of fluid flow through simplified fractures was also implemented and the local and average permeability results based on varying-radius pipeline modelling were compared against those based on direct pore-scale modelling. The fracture after CO_2 exposure in the reactive diffusion process was covered by substantial precipitated calcite, and the permeability of the fracture decreased from 4.15×10^{-8} m^2 to 2.96×10^{-8} m^2. In contrast, the fracture after CO_2 exposure in the reactive flow process underwent significant dissolution, a large number of tensile micro-fractures were formed at the surface of the fracture, and the permeability of the fracture increased from

3.91×10^{-8} m^2 to 4.23×10^{-8} m^2. The relative error of the average fracture permeability obtained from direct pore-scale modelling (-7.33%–4.05%) was comparable with that obtained from varying-radius pipeline modelling (-7.77%–10.64%).

Keywords: Shape-permeability relation; varying-radius pipeline model; direct pore-scale model; X-ray imaging; GCS wellbore cement

1. Introduction

Carbon storage and utilisation in deep geologic formations, such as oil and gas reservoirs, deep saline aquifers, coal seams and salt caverns, provides a feasible solution to mitigating the increase in atmospheric concentration of CO_2 [1]. Wellbore cement sheaths have been identified as potential leakage pathways for CO_2 from reservoirs utilised for GCS [2, 3]. Portland cement is a common sealing material for wellbores of geologic carbon sequestration [4]: Cement annulus is placed between steel casing and formation rocks to prevent fluid migration and provide mechanical support during production [5]; cement plug is placed inside the casing to block the vertical migration of fluids in abandoned well [6].

Fully hydrated Portland cement is consisted of approximately 70% calcium-silicate hydrates (CSH) and 20% portlandite ($Ca(OH)_2$) [3]. When exposed to CO_2-saturated brine, a series of reactions between CO_2 and cement as shown in Eq. 1 occur [7, 8], which can gradually alter the micro-structure of cement. The attack of H^+ on calcium-silicate hydrates and portlandite will generate a more porous cement paste with amorphous silica (SiO_2) as the major component, causing loss of mechanical strength and increase in permeability. Meanwhile, the precipitation of carbonate in high pH pores hinders further propagation of the degradation zone. Therefore, laminated zones including the unaltered zone, a depletion zone, a carbonated zone and a degraded zone presented in sequence from inner cement to cement–CO_2 interface were commonly observed in experiments [9]. Studies have also suggested that the extent of cement alteration depends on existing defects (fractures and voids) and fluid residence time [10-15]: Self-healing of fractures as a result of mineral precipitation was reported in diffusion controlled experiments conditions; opening of fractures was revealed in reactive flow experiments or in cases where large voids and cracks existed.

$$
\begin{aligned}
& CO_2 + H_2O \Leftrightarrow H_2CO_3 \\
& H_2CO_3 \Leftrightarrow H^+ + HCO_3^- \\
& HCO_3^- \Leftrightarrow H^+ + CO_3^{2-} \\
& CSH(s) + 3.6H^+ \Leftrightarrow 1.8Ca^{2+} + SiO_2(am) + 7H_2O \\
& SiO_2(am) \Leftrightarrow SiO_2(aq) \\
& Ca(OH)_2(s) + 2H^+ \Leftrightarrow Ca^{2+} + 2H_2O \\
& CaCO_3(s) \Leftrightarrow Ca^{2+} + CO_3^{2-}
\end{aligned}
\tag{1}
$$

Due to the unevenness in composition and structure of cement and the complexity of reactions, the micro-structure of cement and fracture after exposing to CO_2 solution can be strongly heterogeneous. X-ray imaging has been used to image the complicate 3D structure for analysis of mineralogy alteration [16], porosity and aperture change [17], and for study of fluid flow and evaluation of hydraulic properties of fractures combining the technique of CFD [18]. CFD simulation on reconstructed pore/fracture geometry obtained from X-ray imaging, also known as direct pore-scale modelling, of nonlinear flow for evaluation of permeability or conductance was not uncommon [18-25]. It is known that the accuracy of this method depends highly on the resolution of the CT images or the loyalty of the reconstructed geometry to the real pore/fracture structure. Moreover, the numerical stability of the method relies highly on the size and quality of the mesh elements, and the method can be computationally demanding [26]. In many studies, the high resolution CT images are cropped or downscaled to a small ROI/REV to save computational time [27-29]. Allowing a certain degree of error, Pore Network Model (for porous rock) [30-36] or Pipe Network Model (for fractured rock) [37, 38] is capable of solving large-scale flow problem efficiently using a topologically representative network with idealised properties derived from the underlying image [26]. In conventional Pore Network Model or Pipe Network Model, a pore-throat or fracture segment is simplified into a cylinder tube of constant radius, the hydraulic conductance of the tube can be determined from the radius of the tube based on Poiseuille's equation, and the physics of flow is governed by Darcy's law (linear flow law). It is suggested that the characteristic radius of the idealised cylinder tube for Network Model or Pipe Network Model can be approximated by the inscribed radius (radius of maximal inscribed sphere) [32, 36], the equivalent radius (sqrt(A/π)) [33], and the effective radius (the arithmetic mean of the inscribed radius and the equivalent radius) [35]. Another common idealisation suggests using tubes of elliptical, rectangular or triangular cross-section rather than a circular cross-section, and the shape factor, A/P^2 (related to a dimensionless characteristic radius), is used to predict the dimensionless conductance [30, 31, 34, 36, 39]. The simplification of n-corner star cross-section to represent flow cross-section of complicate shape has also been proposed to predict the conductance using both the shape factor and the inscribed radius of the simplified n-corner star [40]. Neural network–based method has also been proposed to predict dimensionless conductance directly from the circularity ($4\pi A/P^2$) and convexity (A/A_{hull}) of the flow cross-section without shape simplification [19]. While the direct pore-scale modelling is 'loyal to the truth' both in terms of geometry and physics, Pore Network Model or Pipe Network Model simplifies both (geometry and physics), Sisavath et al. (2001) [41] suggested that between these two extreme approaches lies that of solving the Navier–Stokes flow for slowly varying tubes at low Reynolds number using a perturbation analysis. Analytical solution for such model has been derived for axisymmetric tube of sinusoidally varying radius [41, 42].

Geochemical alteration of cement micro-structure, especially fracture morphology, plays a vital role in modifying the flow and transport properties of GCS well. Understanding the changes in fracture morphology under GCS environment and establishing a correlation between fracture topology with hydraulic properties for fast and accurate simulation of fluid flow is essential for prediction of leakage. In this study, X-ray imaging was used to unveil the micro-structural change of pre-fractured cement cores subjected to static CO_2 saturated brine and continuous flow of CO_2 saturated brine. Finite element mesh of the fracture was reconstructed from the CT image, then numerical simulation of single-phase flow through the fracture was carried out for assessment of local and average permeability and conductivity change. The optimal characteristic radius formulation for the fractures was determined from the relation between the shape of fracture cross-sections and the conductivity (permeability) of the cross-sections based on direct pore-scale modelling. The optimal characteristic radius formulation was then deployed to construct a pipe of varying radius as the optimal representation of the fracture. One dimensional Navier–Stokes flow through the reconstructed varying-radius pipe, which is thus termed "varying-radius pipeline modelling" in this study, was implemented to re-evaluate fracture permeability. Findings from this work aim to shed light on micro-structure alteration of defective wellbore cement under GCS environment, and provide implications for development of numerical models to assess permeability evolution and CO_2 leakage.

2. Experiments of CO_2 saturated brine–cement interaction and X-ray imaging

Two types of aqueous CO_2–cement interaction experiments were designed to demonstrate the influence of CO_2 residence time on cement micro-structure alteration under elevated pressure and temperature relevant to carbon sequestration. The reactive-diffusion (RD) type of interaction is related to the experiment where a pre-fractured cement core was immersed in static CO_2 saturated brine, and the reactive-flow (RF) type of interaction is related to the experiment where CO_2 saturated brine penetrated a cement core through an artificial fracture. The pre-fractured cement cores were produced using class G Portland cement through moulding. The cement cores are about 10 mm in diameter and 32 mm in length with a Φ 1 mm fracture running through each core. The cement cores were then cured in 1 wt% NaCl in a mini-reactor under elevated temperature of 62 ℃ and pressure of 17 MPa for 14 days. Curing under elevated pressure and temperature is a necessary process mimicking the casting of oil wellbore cement in a deep well, which is essential to reduce the initial permeability and harden the CSH, and thus improving the resistance against diffusion-driven chemical reactions [6, 43, 44].

2.1 CO_2 saturated brine–cement interaction

In the RD experiment, cement cores were immersed in CO_2 saturated brine in the mini-reactor under the same temperature and pressure for curing. The device for the reactive-diffusion experiment is illustrated in Fig. 1 a, which is comprised of a CO_2 tank, an ISCO pump and a mini-reactor. In the RF experiment, the CO_2 saturated brine was injected in the cement core installed in a flow-through cell (a mini–core holder) at constant flow rate of 0.01 ml/min under elevated temperature of 62 ℃, pore pressure of approximately 17 MPa, and confining pressure of 20 MPa. The device for the reactive-flow experiment is illustrated in Fig. 1 b, which is comprised of a CO_2 tank, three ISCO pumps, a mini-reactor, a flow-through cell, a water bath and two beakers. The main differences of the RD and the RF process are: First, the fluid in the RD process is stagnant, and the fluid flow rate is 0.01 ml/min in the RF process; second, the effective stress in RD process was 0 MPa and in the RF process was 3 MPa; third, both external core surface and internal fracture surface were directly exposed to CO_2 solution in the RD process, only internal fracture surface in the RF process was directly exposed to CO_2, the external core surface covered by rubber sleeve had limited access to

CO_2. Permeability test for cement cores, either from the RD experiment or the RF experiment, was carried out before and after the exposure. The permeability of the fractures were derived by dividing core permeability with the average area fraction of fracture (which was evaluated from the CT images). The result concerning permeability measurement and calculation is provided in Table 1.

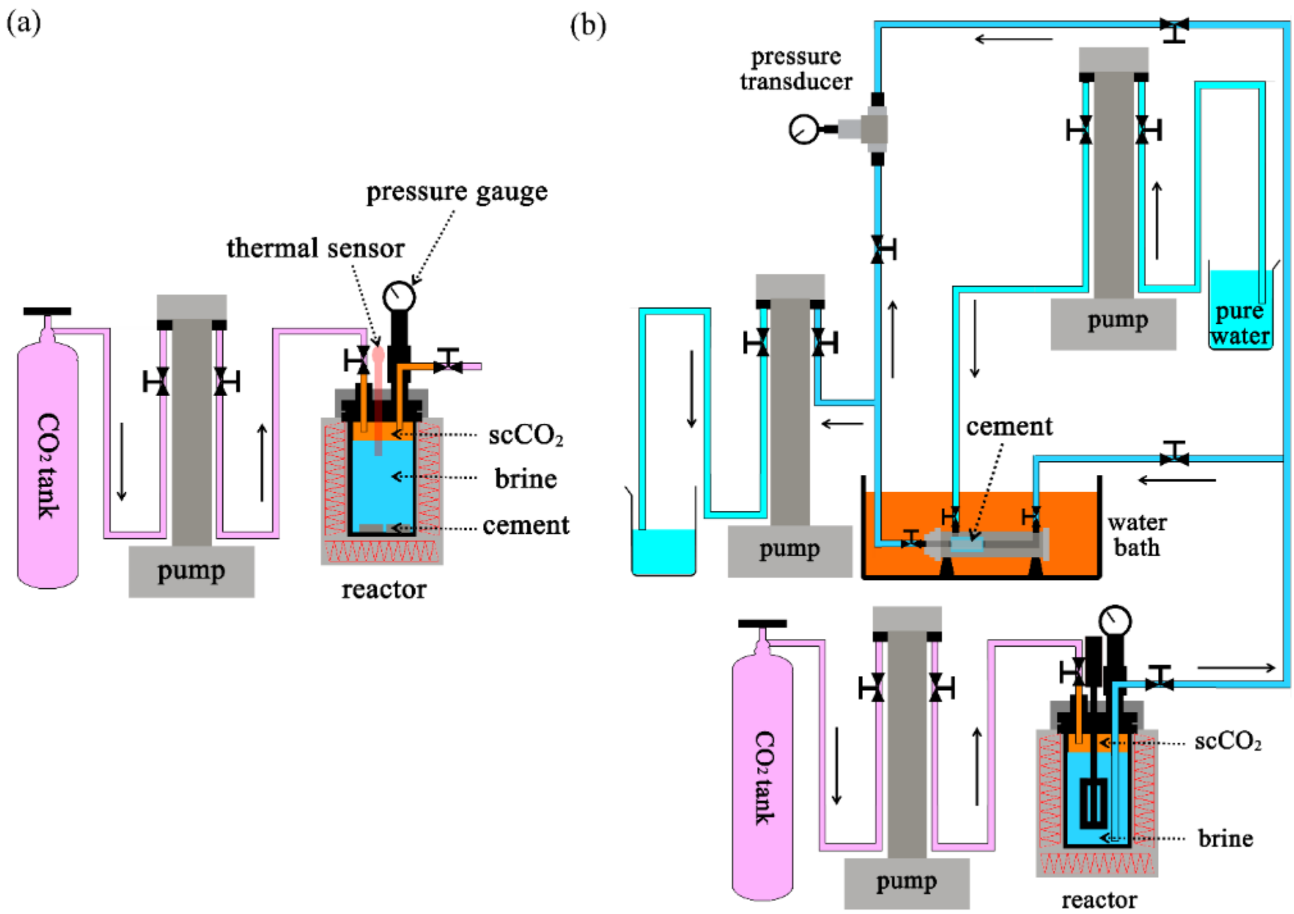

Fig. 1 Device for CO_2 saturated brine–cement interaction experiments: (a) reactive-diffusion experiment; (b) reactive-flow experiment

Table 1 Permeability measurement and fracture permeability evaluation from experiment

Label*	RDD0	RDD14	RFD0	RFD14
κ_{core} (m^2)	6.8027×10^{-10}	4.0741×10^{-10}	5.7215×10^{-10}	8.9566×10^{-10}
A_{frac}/A_{core}	0.016392	0.013764	0.014633	0.021174
κ_{frac} (m^2)	4.15×10^{-8}	2.96×10^{-8}	3.91×10^{-8}	4.23×10^{-8}

* the core or fracture labels represent samples from the reactive-diffusion (RD) experiment or

reactive-flow (RF) experiment before (D0) or after (D14) exposure to high pressure CO_2 saturated brine solution.

2.2 X-ray imaging of cement cores before and after CO_2 exposure

X-ray imaging of the two cement cores, one from the RD experiment and another from RF experiment, was conducted using a Zeiss Xradia Versa 410 CT scanner at the Institute of Rock and Soil Mechanics, Chinese Academy of Sciences. The beam energy was 80 keV/10 W. To attain a high pixel resolution (of approximately 11 μm), each cement core was imaged in four segments and stitched into one CT image. Image registration by the same approach described in the authors' previous paper [16] was employed to align the cement images before and after interaction to facilitated the comparison of local micro-structure and hydraulic properties change when online X-ray imaging was not available.

3. Methodology for image-based estimation of fracture permeability

For direct pore-scale modelling, the pressure profile and velocity field in the pore/fracture domain can be obtained from stationary incompressible Navier–Stokes flow modelling, as expressed in Eq. 2.

$$\begin{cases} (\rho\mathbf{v}\cdot\nabla)\mathbf{v} = \nabla\cdot\left[-p\mathbf{I} + \eta\left(\nabla\mathbf{v} + (\nabla\mathbf{v})^T\right)\right] \\ \nabla\cdot\mathbf{v} = 0 \end{cases}$$
$$\begin{cases} p = p_\mathrm{I} & \Gamma_\mathrm{Inlet} \\ v = q/A_\mathrm{O} & \Gamma_\mathrm{Outlet} \\ \mathbf{n}\cdot\mathbf{v} = 0 & \Gamma_\mathrm{Wall} \end{cases} \tag{2}$$

where $\mathbf{v}$ (m/s) stands for the true fluid velocity; ρ (kg/m^3) and η (Pa·s) are the density and the viscosity of the fluid, respectively; p (Pa) is pore fluid pressure; $\mathbf{I}$ is the 3D identity matrix; $\mathbf{\Gamma}_\mathrm{Inlet}$, $\mathbf{\Gamma}_\mathrm{Outlet}$, and $\mathbf{\Gamma}_\mathrm{Wall}$ denote respectively the inlet, outlet and wall boundaries of the fracture domain.

Assuming the prevailing flow path is along x-axis, given the flow is steady and of low Reynolds number, the flux through an arbitrary fracture segment can be evaluated using Darcy's Law, as expressed in Eq. 3; Poiseuille's equation, or the lubrication approximation for Newtonian creep flow through pipe, can also be used to evaluate the flux of the fracture segment [45, 46], as expressed in

Eq. 4.

$$q_{ij} = -\frac{\kappa_{ij} A_{ij}}{\eta} \frac{\left(p_j - p_i\right)}{\left(x_j - x_i\right)} \tag{3}$$

$$q_{ij} = -\frac{\pi r_{ij}^4}{8\eta} \frac{\left(p_j - p_i\right)}{l_{ij}} = -\frac{\pi r_{ij}^4}{8\eta\tau_{ij}} \frac{\left(p_j - p_i\right)}{\left(x_j - x_i\right)} = -g_{ij} \frac{\left(p_j - p_i\right)}{\left(x_j - x_i\right)} \tag{4}$$

where i and j denote the yz cross-sections at the inlet and outlet of the fracture segment ij; A_{ij}, l_{ij} and r_{ij} represent the area, length, and radius, respectively, of the characteristic capillary tube as an idealisation of the fracture segment; τ_{ij} is the tortuosity of the fracture segment; κ_{ij} is the permeability of the fracture segment; g_{ij} is the hydraulic conductance of the fracture to transport a single-phase fluid with a viscosity of η along x-axis following the pore network model definition. For convenience, we use the term $\kappa_{ij}A_{ij}$ (or ηg_{ij}) to define the intrinsic conductivity of the fracture. Note that the definition is slightly different from the conductivity of planar fracture which is defined as fracture permeability times fracture width. Based on the above definition, the average permeability and conductivity of the fracture can be computed from the following equation,

$$\begin{cases} \kappa_{\mathrm{f}} = -\dfrac{q\eta}{A_{\mathrm{f}}} \dfrac{\left(x_{\mathrm{O}} - x_{\mathrm{I}}\right)}{\left(p_{\mathrm{O}} - p_{\mathrm{I}}\right)} \\ p_{\mathrm{O}} = \dfrac{\int_{\mathrm{A_O}} p\mathrm{d}y\mathrm{d}z}{\int_{\mathrm{A_O}} 1\mathrm{d}y\mathrm{d}z} \quad \left(\dfrac{q}{A_{\mathrm{f}}}\right) = \dfrac{\int_l 1\mathrm{d}x \int_{\mathrm{A}_i} v_x \mathrm{d}y\mathrm{d}z}{\int_l 1\mathrm{d}x \int_{\mathrm{A}_i} 1\mathrm{d}y\mathrm{d}z} = \dfrac{\int_{\mathrm{V_f}} v_x dV}{\int_{\mathrm{V_f}} 1dV} \end{cases} \tag{5}$$

Combining Eq. 3 and Eq. 4, the relation between permeability (or conductivity) and shape of the fracture segment ij can be expressed as in Eq. 6.

$$\left(\eta g_{ij}\right) = \kappa_{ij} A_{ij} = \frac{\pi r_{ij}^4}{8\tau_{ij}} \tag{6}$$

When the cross-section j approaches the cross section i, the permeability of an arbitrary flow cross-section i (κ_i) can be computed from the partial differential form of Eq. 3, the relation between permeability (or conductivity $\kappa_i A_i$) and shape of the cross-section i can be derived following Eq. 6. The formulation to evaluate cross-sectional permeability and the relation between cross-sectional permeability and shape of the cross-section is presented in Eq. 7.

$$\begin{cases} \boldsymbol{\kappa}_i = -\boldsymbol{\eta}\left(\dfrac{q}{\mathrm{A}_i}\right)\left(\dfrac{\partial p}{\partial x}\right)_i^{-1} \\ \boldsymbol{\kappa}_i \mathrm{A}_i = \dfrac{\pi r_i^4}{8\boldsymbol{\tau}_i} \end{cases} \tag{7}$$

where κ_i, A_i and r_i are the permeability, characteristic area and characteristic radius, respectively, of the fracture cross-section i; $(\partial p/\partial x)_i$ represents the average pressure gradient of of the fracture cross-section. By introducing the concept of point permeability expressed as:

$$\boldsymbol{\kappa}_{iP} = -\boldsymbol{\eta}\left(\frac{\partial p}{\partial x}\right)_{ip}^{-1} v_x \qquad (8),$$

the permeability for cross-section i can be addressed numerically using Eq. 9.

$$\boldsymbol{\kappa}_i = \frac{\int_{\mathrm{A}_i} \boldsymbol{\kappa}_{iP}\,\mathrm{d}y\mathrm{d}z}{\mathrm{A}_i} = -\boldsymbol{\eta}\frac{\int_{\mathrm{A}_i}\left(\dfrac{\partial p}{\partial x}\right)_{ip}^{-1} v_x \mathrm{d}y\mathrm{d}z}{\int_{\mathrm{A}_i} 1\mathrm{d}y\mathrm{d}z} \tag{9}$$

Local hydraulic tortuosity of cross-section i can be approximated using the proportion of the average velocity magnitude of cross-section i to the average x-component velocity magnitude of cross-section i as in Eq. 10. Since the fractures (produced by inserting a tube in the cement slurry during moulding) are almost straight geometrically, it is assumed that the hydraulic tortuosity of the fractures is also constant along the x-axis. The assumption is further validated in sub-section 4.4.

$$\frac{1}{\boldsymbol{\tau}_i} \approx \cos\left(\overline{\mathbf{v}}_i, \mathbf{n}_x\right) = \frac{v_{ix}}{\left|\mathbf{v}_i\right|} = \frac{\int_{\mathrm{A}_i} \dfrac{v_x}{v} dA}{\sqrt{\left(\int_{\mathrm{A}_i} \dfrac{v_x}{v} dA\right)^2 + \left(\int_{\mathrm{A}_i} \dfrac{v_y}{v} dA\right)^2 + \left(\int_{\mathrm{A}_i} \dfrac{v_z}{v} dA\right)^2}} \tag{10}$$

Since the inscribed radius, area and perimeter of the flow cross-section are considered crucial factors in predicting the conductance of fracture or pore throat in Pore Network Model or Pipe Network Model, the authors intended to seek an optimal characteristic radius of the fracture from the generalised average of three types of equivalent radius that are directly related to the inscribed radius, area and perimeter of the flow cross-section, as presented in Eq. 11. The first equivalent radius is the radius of the maximal inscribed sphere, the second equivalent radius is a measure of flow area, and the third equivalent radius, also known as the hydraulic radius in channel flow, is a measure of the flow area and wetted perimeter. The optimal formulation of the characteristic radius is found when the distance between the conductivity evaluated from Darcy's law and the conductivity evaluated from Poiseuille's equation is minimal, which can be described by the optimisation problem as in Eq. 12. A correction of the Poiseuille's equation to allow a conductivity offset by b and to relieve the gradient constraint (i.e. to allow $c \neq 1$) is incorporated in Eq. 12 to take into account the influence of fracture tortuosity and the deviation of image-based shape measurement from that measured from the geometrical mesh. Once the formulation of optimal characteristic radius is established, the fracture can be simplified as a tube of varying characteristic radius using the inscribed radius, area and perimeter of sampled flow cross-sections. The 1D Navier–Stokes flow over the varying-radius pipe representation of fracture, which is referred to as varying radius pipeline modelling in this study, can then be implemented to re-evaluate the conductivity and permeability of the fracture.

$$\begin{gathered} R_{\mathrm{EQU1}} = R_{\mathrm{INS}} \quad R_{\mathrm{EQU2}} = \sqrt{\frac{\mathrm{A}}{\pi}} \quad R_{\mathrm{EQU3}} = \frac{2\mathrm{A}}{\mathrm{P}} \\ R = \left[\sum_{i=1}^{3} a_i R_{\mathrm{EQU}i}; \quad \left(\sum_{i=1}^{3} a_i R_{\mathrm{EQU}i}^{4} \right)^{\frac{1}{4}}; \quad \prod_{i=1}^{3} R_{\mathrm{EQU}i}^{a_i} \right] \end{gathered} \tag{11}$$

$$\begin{gathered} \text{objective} \quad \min \left[\kappa \mathrm{A} - b \frac{\pi R^4}{8} - c \right]^2 \\ \text{constraint} \quad \begin{cases} \sum_{i=1}^{3} a_i = 1 \\ 0 \le a_i \le 1 \end{cases} \end{gathered} \tag{12}$$

4. Results and discussion

4.1 Micro-structure alteration unveiled by CT images

The orthogonal images of the two cement cores are shown in Fig. 2. The difference map revealing local grayscale alteration is also presented in Fig. 2 to demonstrate the performance of image registration. As it can be seen, the CO_2–cement interaction was more intense in the RF experiment. Large amount of dissolution due to H^+ attack was observed on the surface of the fracture in the RF experiment; the external surface of the core, covered by rubber sleeve, however, was dominated by precipitation. In contrast to the core in the RF experiment, a large amount of calcite had precipitated on the fracture surface in the RD experiment, rendering a high frequency and low amplitude variation in fracture roughness; the external surface of the core, which was directly exposed to bulk CO_2 solution, was distinguished by substantial dissolution. Distinctive laminated layers of degradation, carbonation and depletion commonly observed in aqueous CO_2–cement interaction experiments were also discovered on the "surface of dissolution" (i. e. the fracture surface in the RF experiment and the core's external surface in the RD experiment); however, the degradation layer in the RF experiment was much thicker than that in the RD experiment, and the carbonate layer in the RF experiment was much looser than that in the RD experiment. This suggests that the laminated micro-structure in the RF experiment might be weaker than that in the RD experiment. Proof of weaker micro-structure was also revealed by significant micro-fractures on the surface of the fracture in the RF experiment, while almost no micro-fracture was observed on the external surface of the cement core in the RD experiment. The micro-fractures in the RF experiment are distinguished by a large amount of radial tensile micro-fractures and a small amount of axial shear-tensile micro-fractures at the half of the core adjoining the inlet. The development of these micro-fractures could be a result of uneven mechanical loading over heterogeneous chemical degradation which will require further hydro-chemo-mechanical coupled analysis.

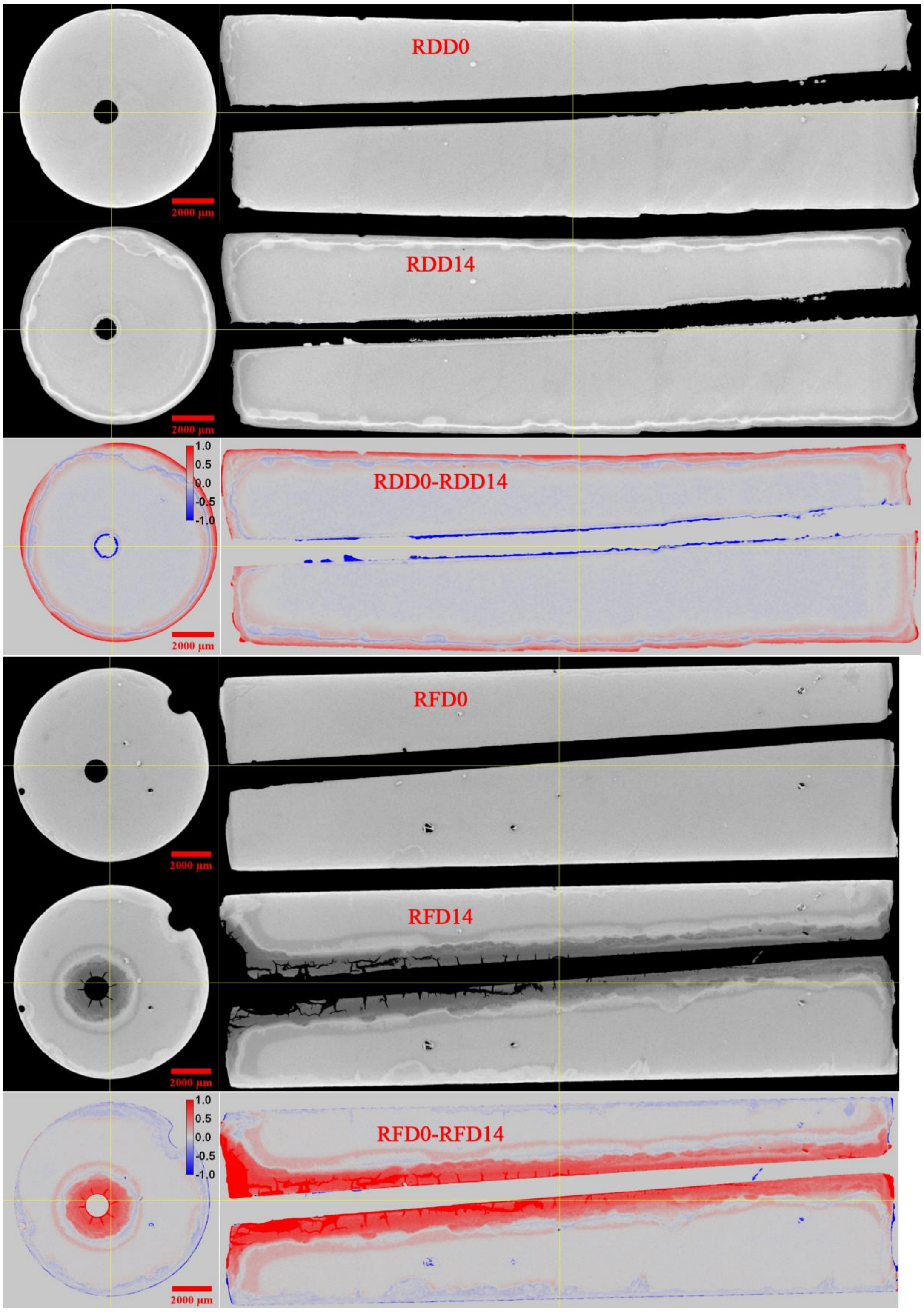

Fig. 2 X-ray CT images of cement cores before exposure to CO_2 and after exposure to CO_2. Each post-exposure core image is registered to its corresponding pre-exposure core image, and the difference image is obtained by subtracting the pre-exposure core image with the post-exposure core image. Note that the colour scale is normalised by the maximal of the absolute difference grayscale value.

4.2 Direct pore-scale modelling based on virtual fracture geometry

The 3D binary image of the fracture was segmented from the CT image of the cement core by thresholding after smoothing with 3D Gaussian blur (filter window size/image size is 2/1000); trimming of unconnected components was implemented to render a one-connected region; the reconstructed 3D binary fractures before and after exposure from the RD experiment and the RF experiment are presented on Fig. 3.

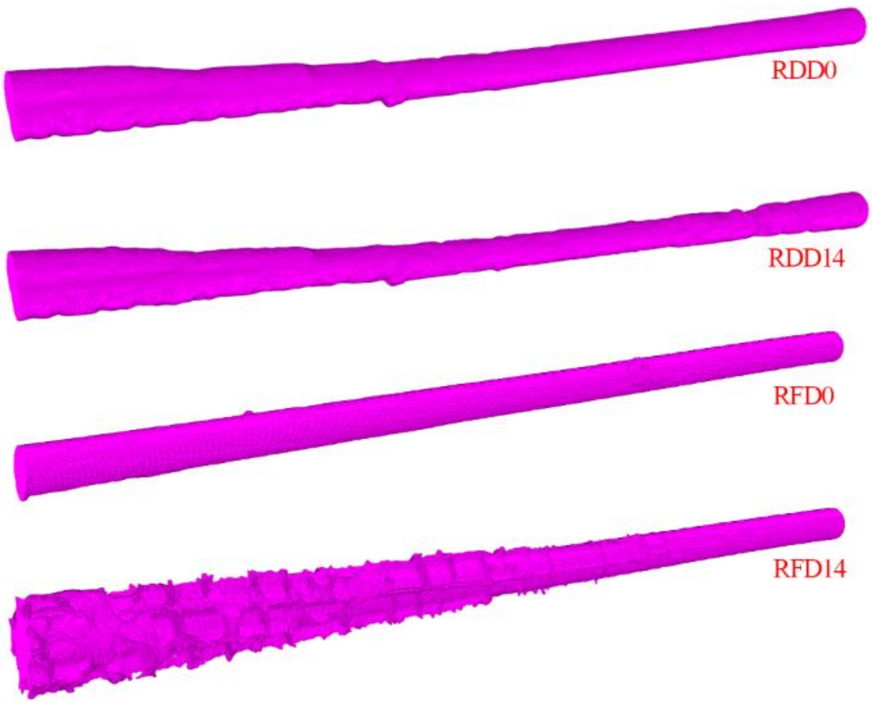

Fig. 3 Reconstructed 3D binary fractures from X-ray CT images of cement cores.

The surface mesh of the fracture was obtained by implementing the marching cubes surface reconstruction algorithm on the 3D binary fractures using the open-source image processing software FIJI/ImageJ [47]. After mesh cleaning, repairing and simplification using the open-source 3D triangular meshes processing software MeshLab [48], the surface mesh was then imported into Comsol Multiphysics to generate the 3D geometry of fracture. It is worth noting that the 3D fracture geometries (as shown in Fig. 4) are not 100% loyal to the real fractures due to limited CT resolution, image smoothing, and mesh simplification, however, smoothing and simplification are necessary procedures to improve local mesh quality for convergence and also to enhance the speed of computation. The guideline to mesh simplification here was a balance among mesh quality, capacity of computation facility and loyalty to structure detail. Simulation of incompressible Navier–Stokes flow through the reconstructed fracture geometry under an inlet pressure of 17 MPa and flow rate of 0.01 ml/min was implemented. The result exhibiting velocity streamline (colour coded by the magnitude of the velocity) through the fractures is plotted in Fig. 4. The Reynolds number for the flow through all fracture geometries was approximately 0.1; this means the Poiseuille's equation suitable for creep flow (Reynolds number <1) should stand valid for the numerical investigation.

The profiles of x-component velocity magnitude and the point permeability (along the x-axis) defined in Eq. 9 on three cross-sections of each fracture geometry are illustrated in Fig. 5. Comparing among different cross-sections, it is observed that higher average velocity magnitude occurs where the average permeability is lower, indicating strong relation of permeability to flow area (when the flow rate is constant the average velocity is determined by flow area). Looking at each fracture cross-section, it is discovered that higher point velocity magnitude occurs where the point permeability is higher; the contour of velocity magnitude is consistent with the contour of point permeability, in spite of small fluctuation; moreover, the value of point permeability shows strong dependence on the distance of the point to the wall, indicating strong relation of permeability with inscribed radius. It is also revealed on Fig. 5 that although the RFD14 cross-section at $x = 0.05$ L is large, substantial region of the cross-section is characterised by slow flow. This is because the large cross-section area also has a small maximal inscribed sphere due to steep variation in the morphology (further proof can be found in Fig. 7).

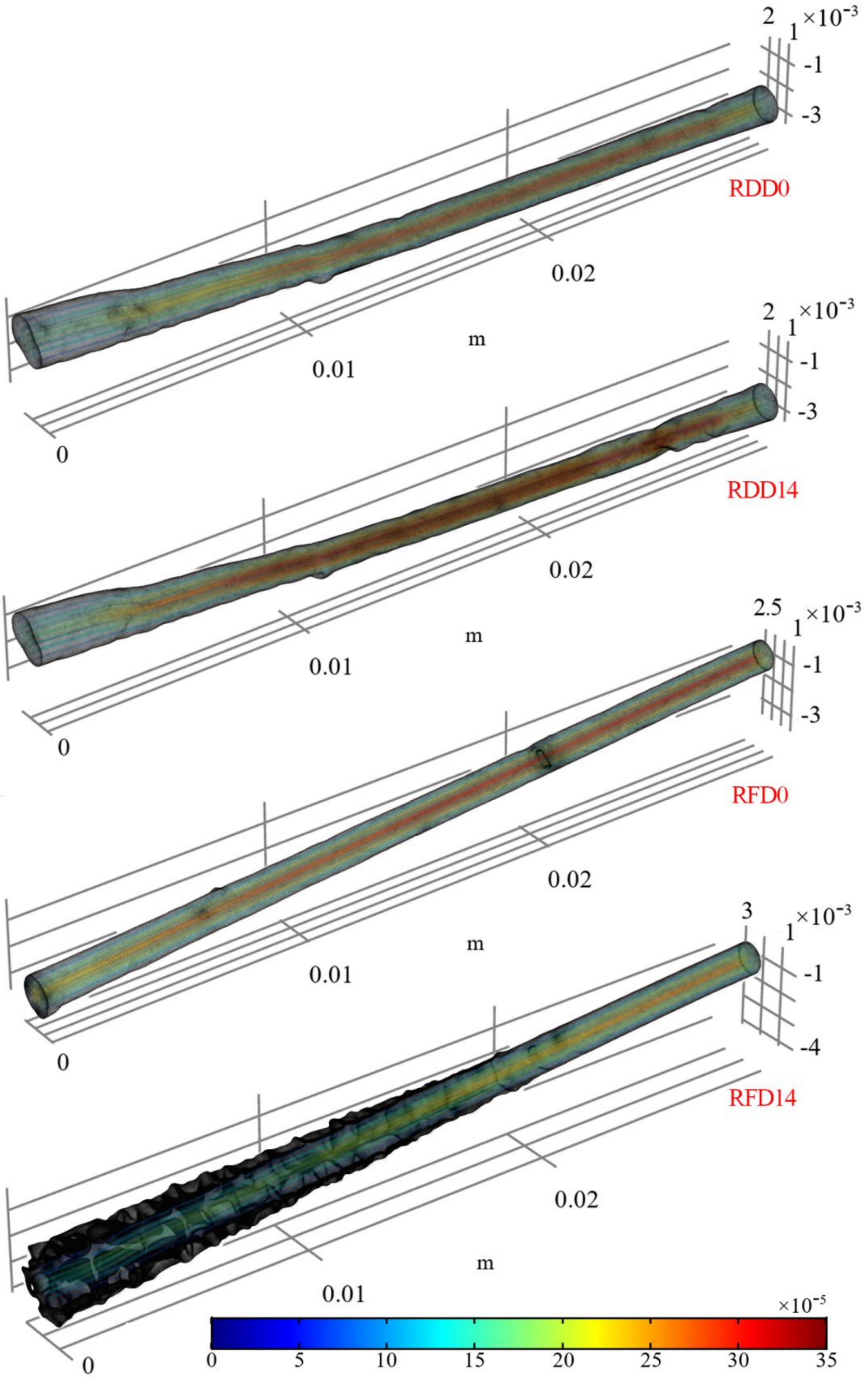

Fig. 4 Demonstration of 3D fractures and velocity streamline.

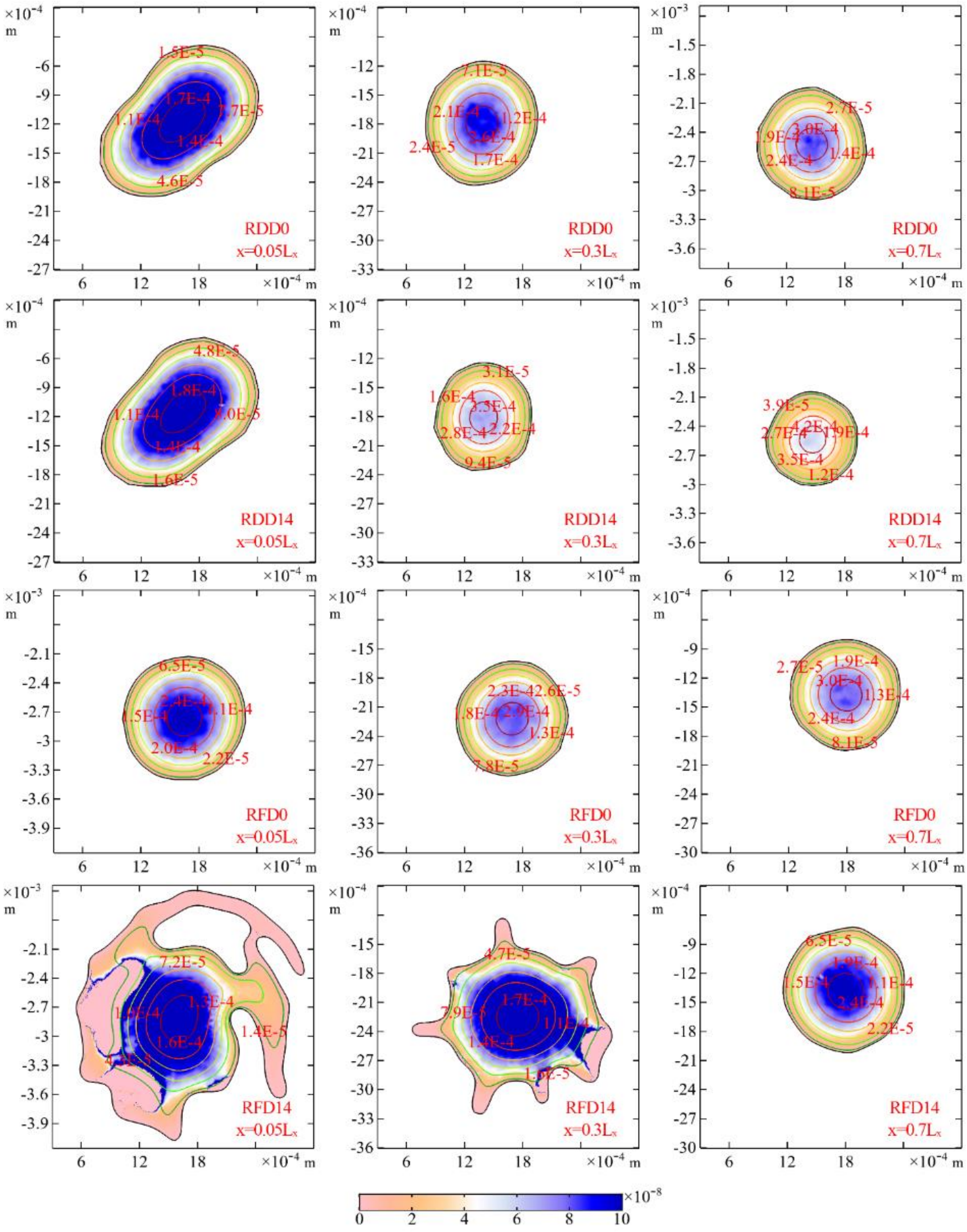

Fig. 5 Profiles of velocity and point permeability for the fracture in each sample. The contour surface is colour coded by the value of point permeability (along the x-axis) defined in Eq. 9, the contour line is colour coded by the magnitude of x-component velocity.

4.3 Permeability and shape relation

4.3.1 Visualisation of morphology and permeability relation

The change in fracture shape, measured by cross-sectional area (A), perimeter (P) and inscribed radius for the virtual fractures (R_{EQU1}) is illustrated in Fig. 6 a & b; it should be noted that the topological data in Fig. 6 is sampled from 19 cross-sections at an interval of $0.05 \times L$ of each fracture. Although the virtual geometry is not loyal to the original image, the topological data is still capable of capturing the morphological change of the fracture: First, the virtual fracture in the RD process had shrunk after exposure and expanded after exposure in the RF process; second, the change of cross-section shape in the RF process is distinguished at the half of the fracture adjoining the fluid inlet and the change of cross-section shape in the RD process is relatively mild. The topological data also suggests that despite significant change in the cross-sectional area and perimeter in the RF process, the change of inscribed radius for the fracture is small. The change in the hydraulic tortuosity of the fractures is plotted in Fig. 6 c, showing small variation of tortuosity value roughly between 1 and 1.01, indicating the assumption of constant tortuosity is acceptable.

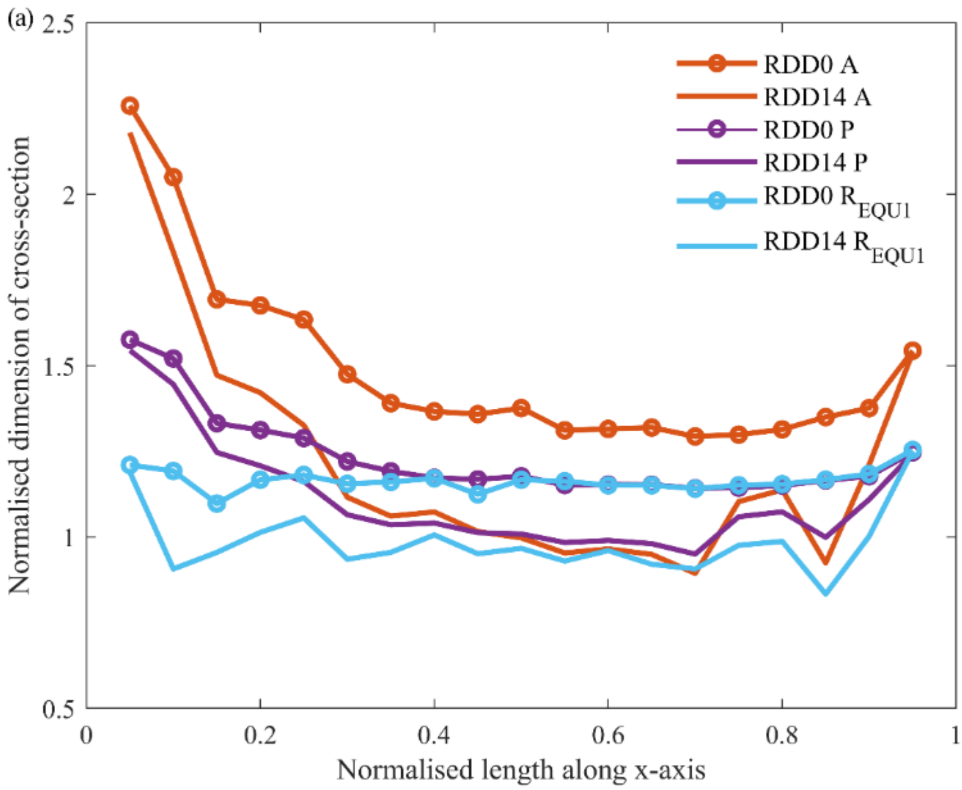

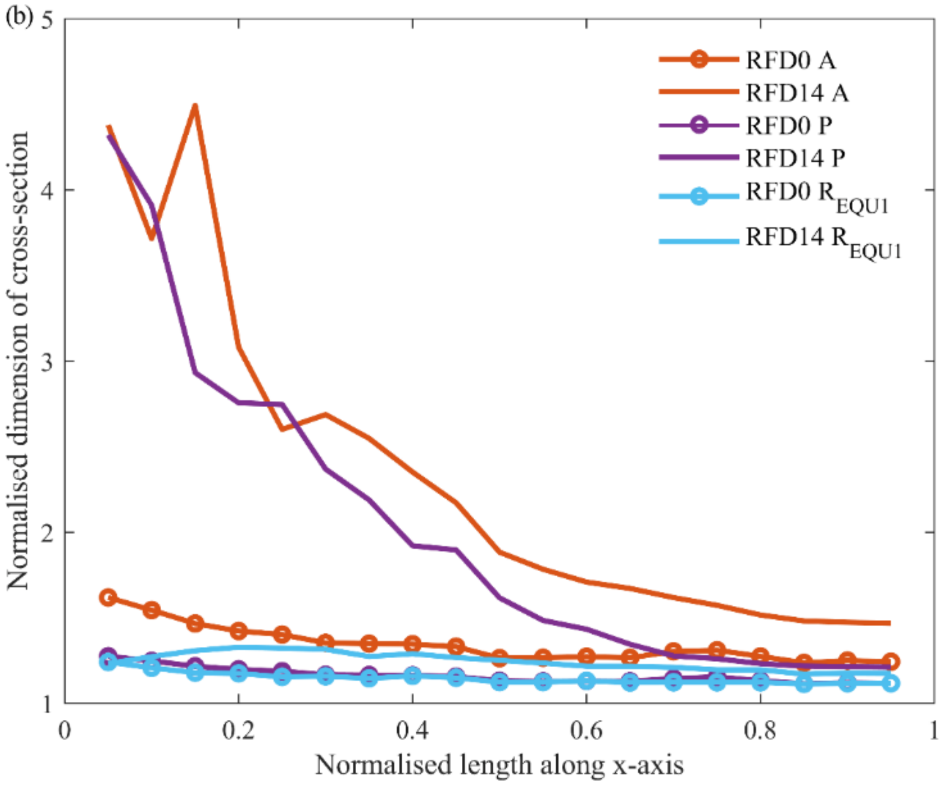

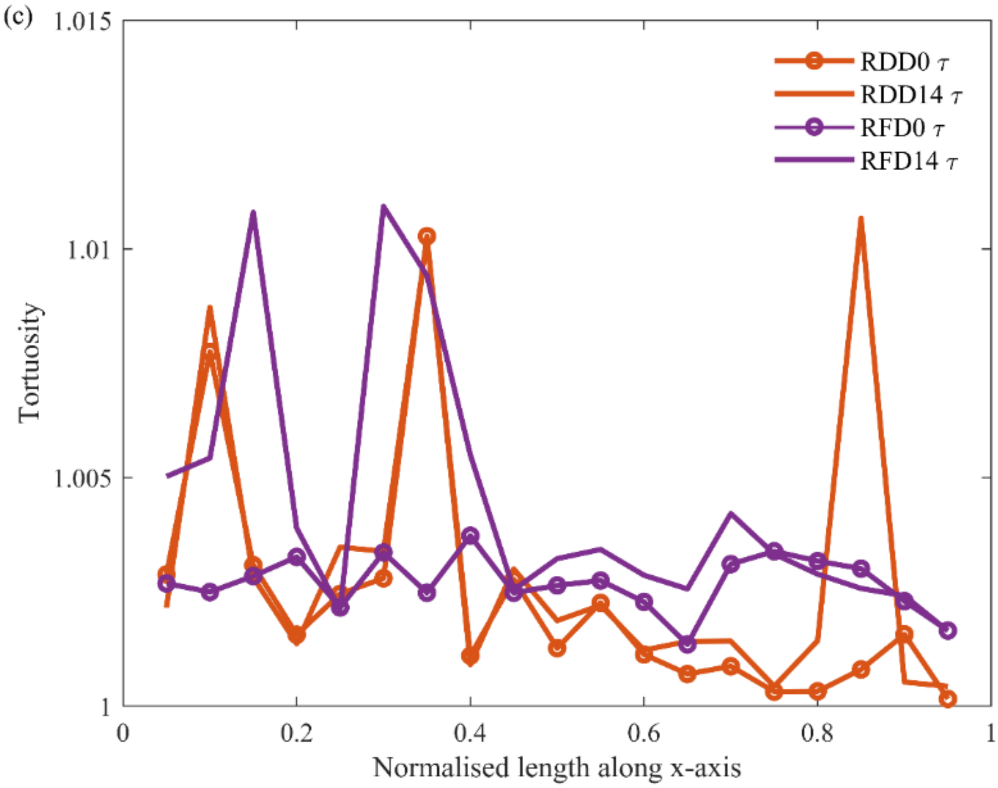

Fig. 6 Alteration of fracture shape described by cross-sectional area, perimeter and inscribed radius for (a) fracture in RD experiment and (b) fracture in RF experiment; (c) alteration of local hydraulic tortuosity for fractures in both the RD and RF experiments; value of cross-sectional area perimeter

and inscribed radius is normalised by the area, perimeter and inscribed radius respectively of a Φ 1 mm circle for better comparison in one figure.

The change in cross-sectional permeability and conductivity for the virtual fractures sampled from the same 19 cross-sections is shown in Fig. 7. The spatial variation in cross-sectional permeability is more in line with the change of area and perimeter. The cross-sectional permeability for the virtual fracture RFD14 shows large variation, especially at the half near the fluid inlet, due to developed micro-fractures that significantly break the continuity of the fracture as revealed on Fig. 7 b. The average permeability for the fractures before and after interaction are 4.09×10^{-8} m^2, 3.08×10^{-8} m^2, 3.86×10^{-8} m^2, 3.92×10^{-8} m^2 respectively for RDD0, RDD14, RFD0 and RFD14. It is worth noting that the average permeability is higher than the minimum of the cross-sectional permeability in all virtual fractures. In general, the permeability of the fracture in the RD process had decreased after exposure and had increased after exposure in the RF process.

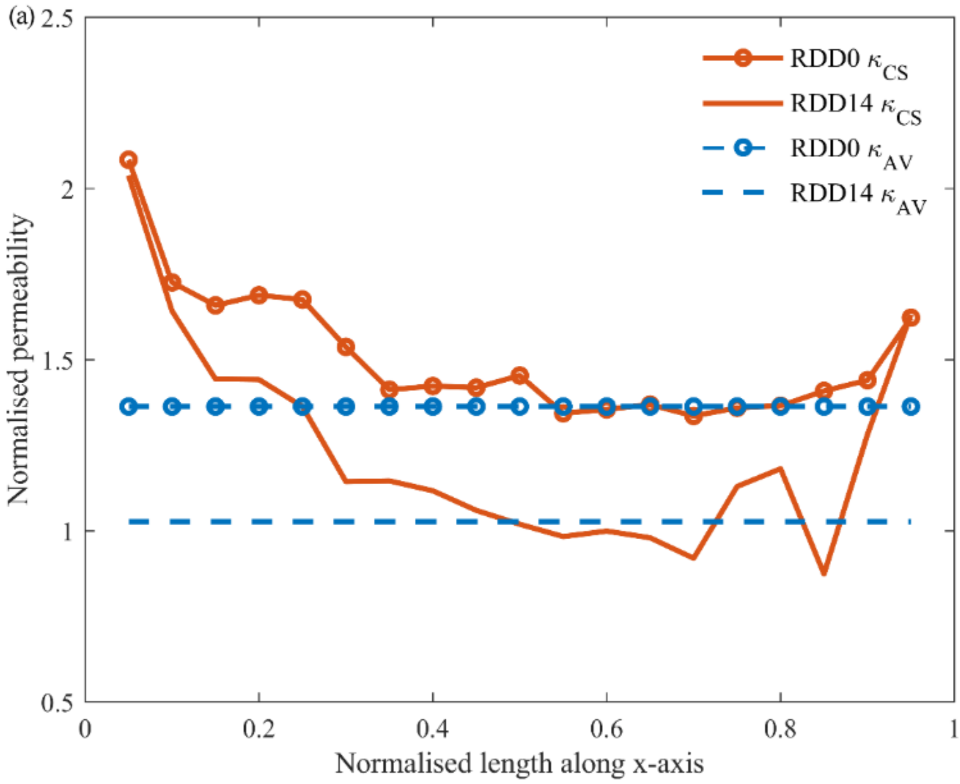

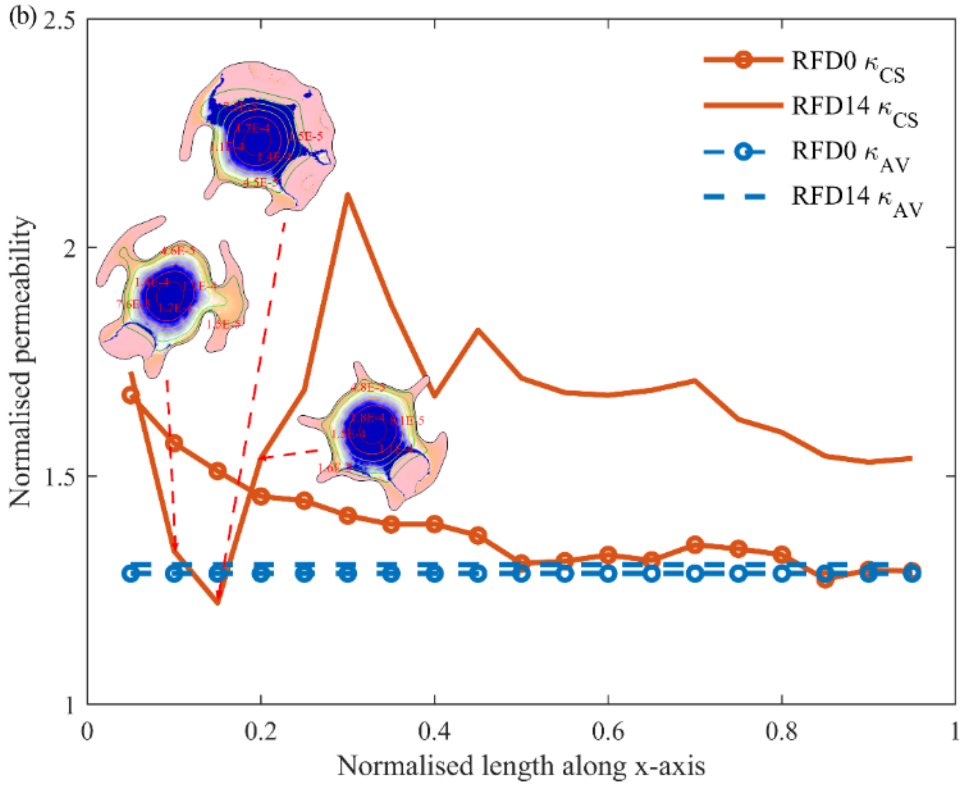
(b)
Normalised permeability
Normalised length along x-axis
RFD0 κ_{CS}
RFD14 κ_{CS}
RFD0 κ_{AV}
RFD14 κ_{AV}
1
1.5
2
2.5
0
0.2
0.4
0.6
0.8
1

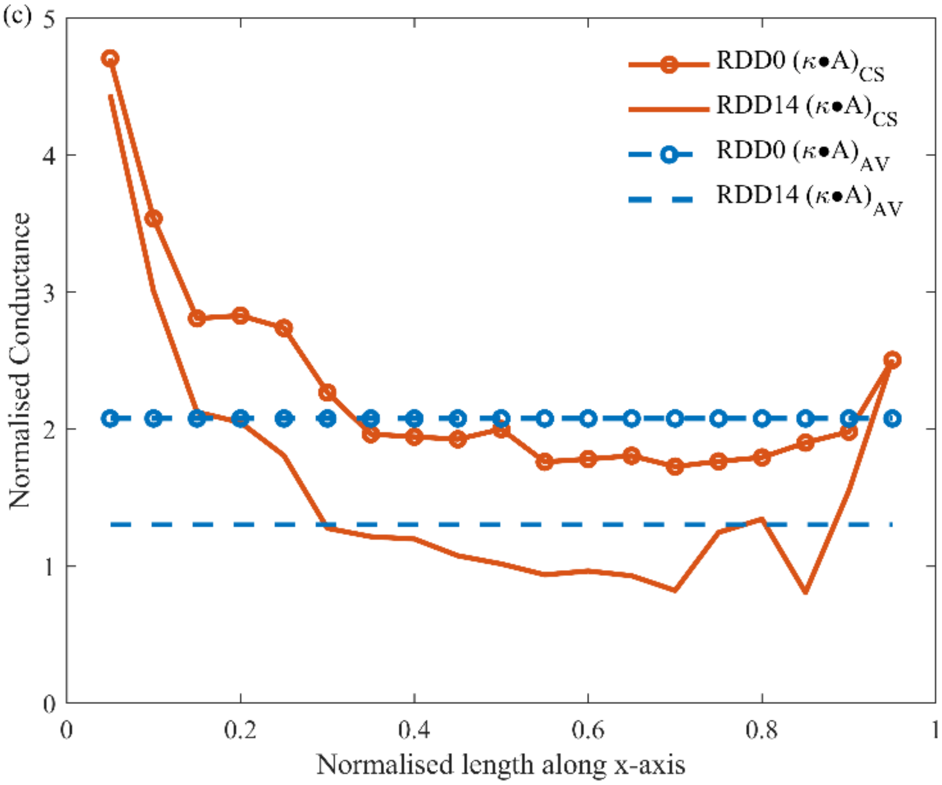
(c)
Normalised Conductance
Normalised length along x-axis
RDD0 $(\kappa \bullet A)_{CS}$
RDD14 $(\kappa \bullet A)_{CS}$
RDD0 $(\kappa \bullet A)_{AV}$
RDD14 $(\kappa \bullet A)_{AV}$
0
1
2
3
4
5
0
0.2
0.4
0.6
0.8
1

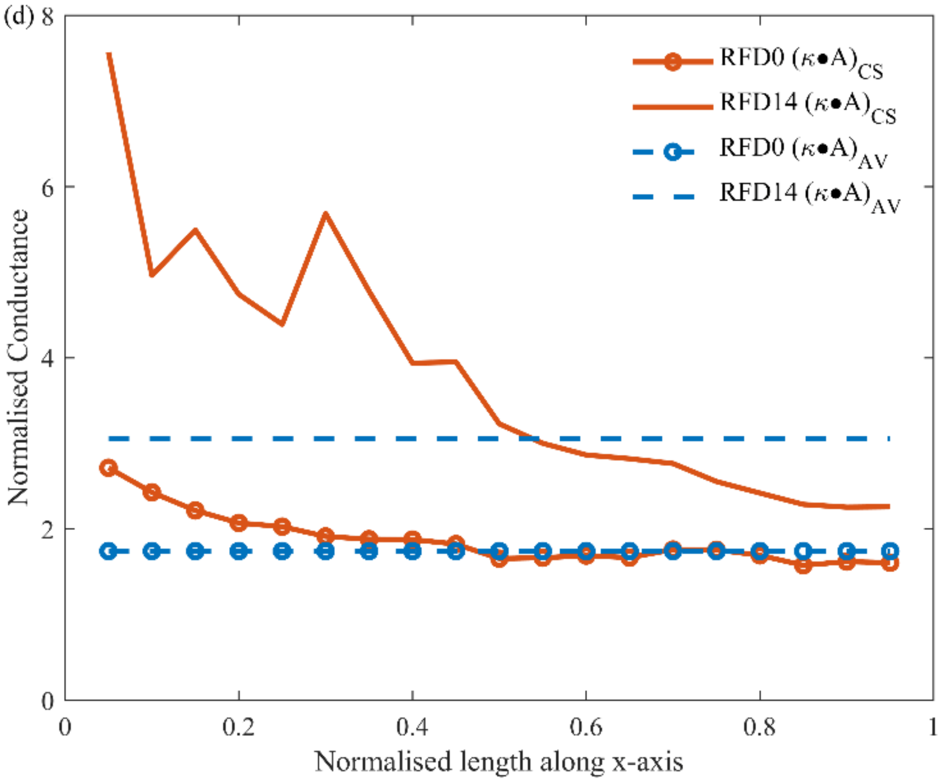

Fig. 7 Alteration of cross-sectional permeability and conductivity of virtual fractures: (a) cross-sectional permeability for cement core from RD experiment; (b) cross-sectional permeability for cement core from RF experiment; (c) cross-sectional conductivity for cement core from RD experiment; (b) cross-sectional conductivity for cement core from RF experiment; value of cross-sectional permeability and conductivity is normalised by the permeability and conductivity respectively of a Φ 1 mm circle.

Three types of equivalent radius (as presented in Eq. 11) and the effective radius ((R_{EQU1}+R_{EQU2})/2) for the cross-sections of the virtual fractures were determined from the inscribed radius, area and perimeter of the cross-sections. The relation of the cross-sectional conductivity ($\kappa \cdot A$) to the different types of radius ($R_{\mathrm{EQU}i}$) is visualised in Fig. 8. Expressions of the linear fitting curves and the performance of the fitting models are presented in Table 2. Based on the scatterplots in Fig. 8, these different types of radius show relatively convincing positive correlation with conductivity. According to the RMSE and R^2_{adj} value in Table 2, the second equivalent radius has the strongest correlation with conductivity, the third equivalent radius has the weakest correlation with conductivity, and the conductivity prediction using effective radius is generally no better than the prediction using the first or second equivalent radius alone. Based on the fitting performance in Fig. 8, all fitting models perform poorly for the conductivity-radius point clouds sampled from the RFD14; taking the point clouds of RFD14 out of the picture, the third equivalent radius could be the best predicator of conductivity.

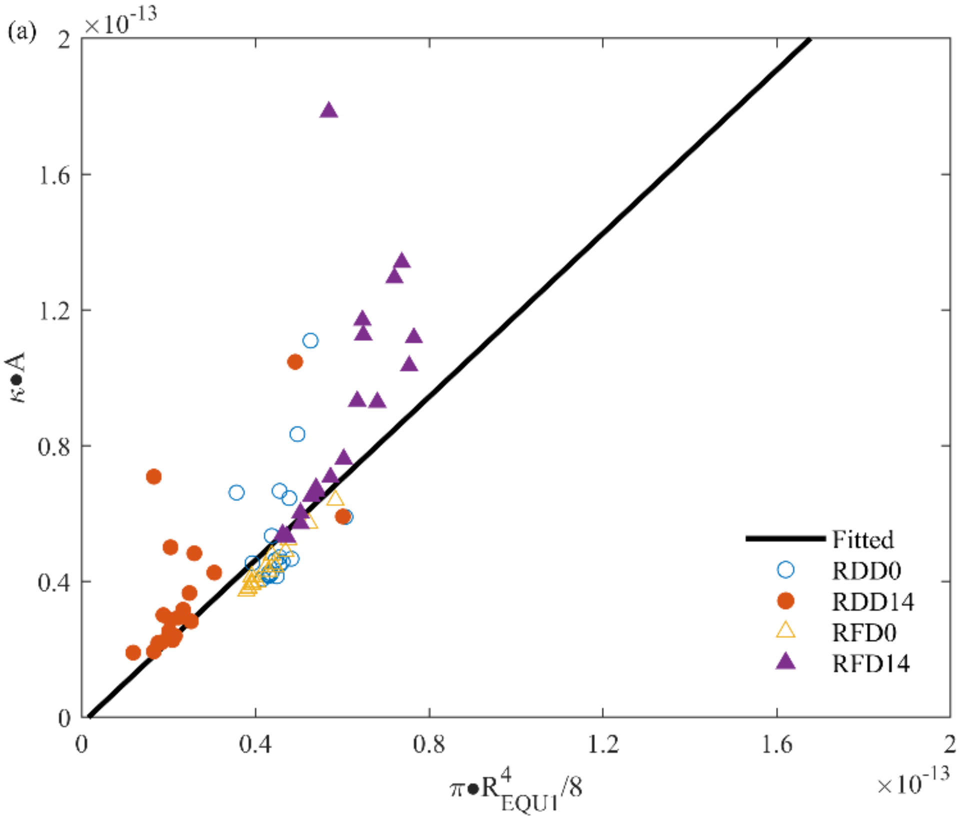

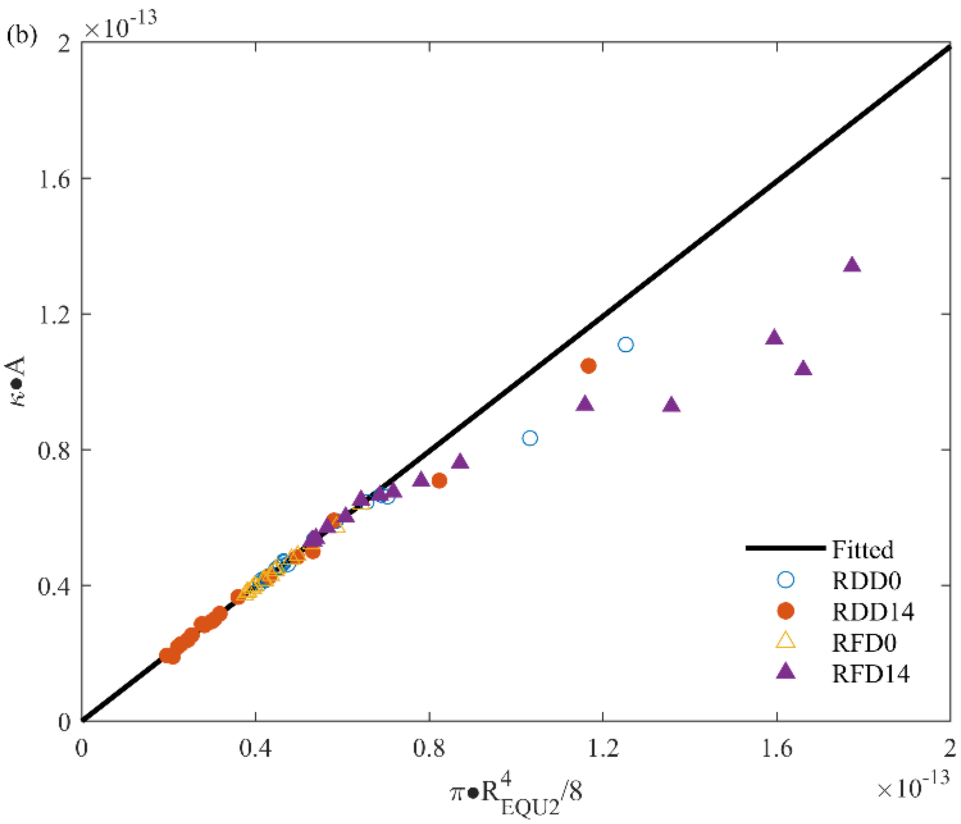
(b)
×10-13
κ•A
π•R4EQU2/8
×10-13
Fitted
RDD0
RDD14
RFD0
RFD14
0
0.4
0.8
1.2
1.6
2

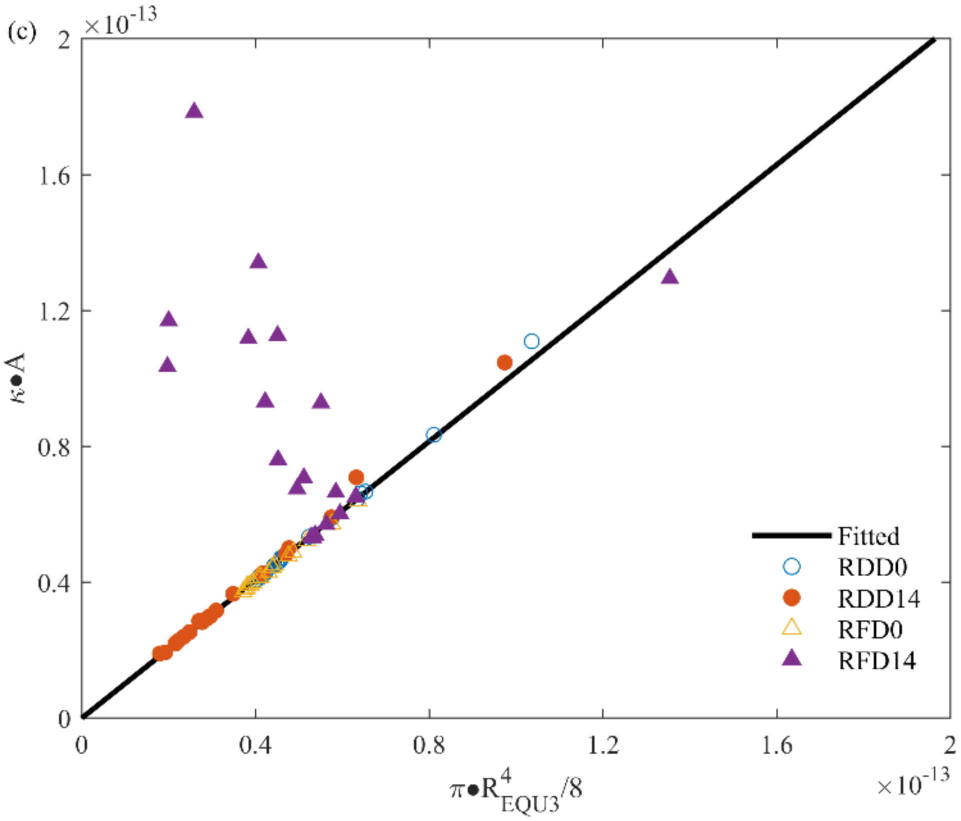
(c)
×10-13
κ•A
π•R4EQU3/8
×10-13
Fitted
RDD0
RDD14
RFD0
RFD14
0
0.4
0.8
1.2
1.6
2

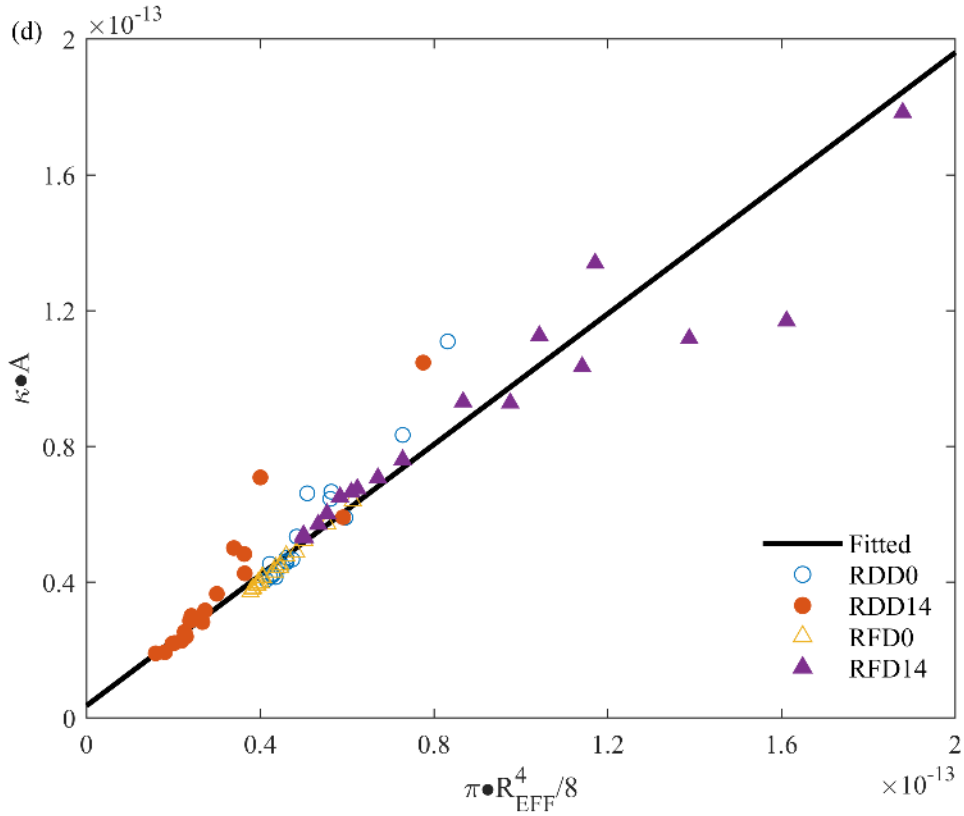

Fig. 8 Correlation between conductivity and equivalent radius: (a) the first equivalent radius (the inscribed radius); (b) the second equivalent radius (sqrt(A/π)); (c) the third equivalent radius ($2A/P$); (d) the effective radius (($R_{EQU1}+R_{EQU2}$)/2).

Table 2 Linear fitting model and fitting performance for correlation between fracture conductivity and different types of equivalent radius

Fitting Equation	$f(X)=bX+c \quad X=\dfrac{\pi R^4}{8}$			
R	*B*	*c*	RMSE	R^2_{adj}
R_{EQU1}	1.2041	-1.8906e-15	4.4071e-15	0.9782
R_{EQU2}	9.9418	9.3466e-18	3.4266e-15	0.9868
R_{EQU3}	1.0186	-1.2359e-17	6.0221e-15	0.9592
R_{EFF}	9.6235	3.6148e-15	4.4910e-15	0.9773

4.3.2 Optimisation of characteristic radius formulation

In search for a reliable characteristic radius representation, optimisation of the characteristic radius formulation based on the ideal relation of conductivity with characteristic radius as proposed in Eq. 11 was carried out. Different characteristic radius formulations derived from the optimisation and the RMSE of each formulation are provided in Table 3. Performance of the three best characteristic radius formulations (highlighted in italic font in Table 3) in predicating the conductivity is demonstrated in Fig. 9.

Table 3 Characteristic radius formulations derived from optimisation and performance of the formulations in predicating conductivity

Optimisation objective	$\min\left[\boldsymbol{\kappa}\mathrm{A}-b\dfrac{\pi R^4}{8}-c\right]^2$					
R	a_1	a_2	a_3	b	c	RMSE
$\sum_{i=1}^{3} a_i r_{\mathrm{EQU}i}$	0.5479	0.4093	0.0428	1.0680	-1.9114E-16	4.8186E-15
	0.5943	*0.4057*	*0*	*1.0017*	*2.1726E-15*	*2.4165E-15*
	1.0000	0	0.0000	1.2041	-1.8906E-15	4.4071E-15
	0	0.4622	0.5378	0.9870	6.6792E-16	3.8297E-15
$\left(\sum_{i=1}^{3} a_i r_{\mathrm{EQU}i}^4\right)^{1/4}$	0.5884	0.2560	0.1556	1.1253	-1.9727E-15	5.4607E-15
	0.7443	*0.2557*	*0*	*1.0326*	*1.7114E-15*	*2.6284E-15*
	0.8531	0	0.1469	1.0844	1.5370E-15	8.7149E-15
	0	0.2852	0.7148	1.0157	-2.5549E-16	3.4611E-15
$\prod_{i=1}^{3} r_{\mathrm{EQU}i}^{a_i}$	0.1689	0.5903	0.2408	1.0126	1.5524E-16	3.0207E-15
	0.3968	*0.6032*	*0*	*0.8699*	*6.2384E-15*	*2.4912E-15*
	0.6919	0	0.3081	1.1360	-1.1074E-15	4.8140E-15
	0	0.6421	0.3579	0.9641	1.4822E-15	3.5759E-15

According to the RMSE of each optimisation in Table 3, similar conclusion that the first equivalent radius and the second equivalent radius have more significant influence on the hydraulic conductivity can be arrived: The optimised characteristic radius formulation using the combination the first equivalent radius and the second equivalent radius generally prevails the optimised characteristic radius formulations using other combinations of the three types of equivalent radius.

The optimal characteristic radius representation approximated by $0.5943 \cdot R_{EQU1} + 0.4057 \cdot R_{EQU2}$ renders a minimal RMSE of 2.4165E-15. Compared to the effective radius which is the arithmetic mean of the first and the second equivalent radius, the optimal characteristic radius formulation suggests the weight of the first equivalent radius be higher than that of the second equivalent radius. It is unveiled from Fig. 9 a that the points beneath the fitting curve are more concentrated and the points over the fitting curve are more dispersed. As it can be deduced, if the optimal characteristic radius formulation was used to estimate the conductivity, the probability of underestimation is larger than overestimation. It is also observed that the second best candidate (with an RMSE slightly higher than the optimal characteristic radius formulation) for the characteristic radius is $R_{EQU1}^{0.3968} \cdot R_{EQU2}^{0.6032}$, which suggests the weight of second equivalent radius be higher than the first equivalent radius; however, the slope for the linear relation of the second best characteristic radius candidate and the conductivity is 0.8699, which is far from what the 'slightly deviating from 1' is expected.

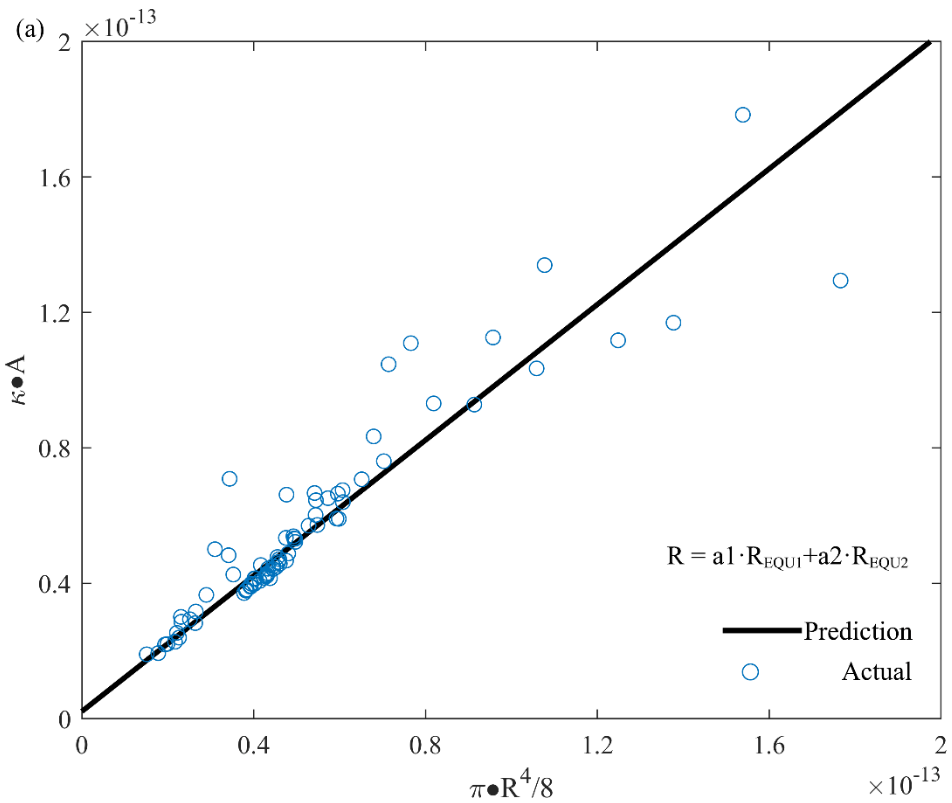

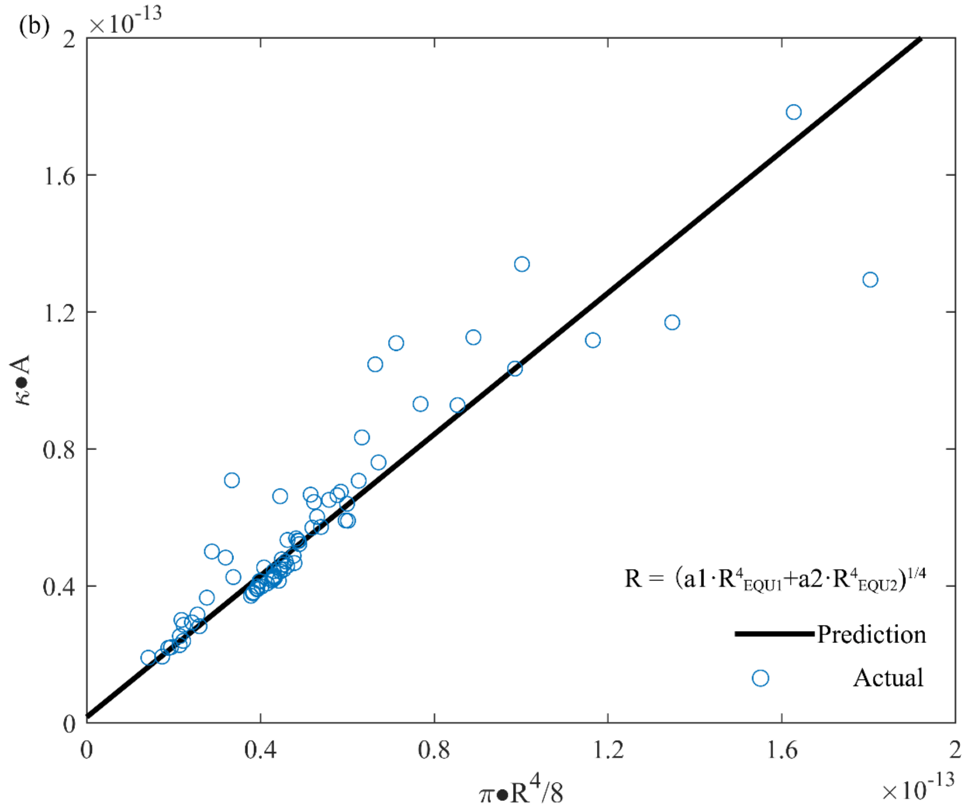

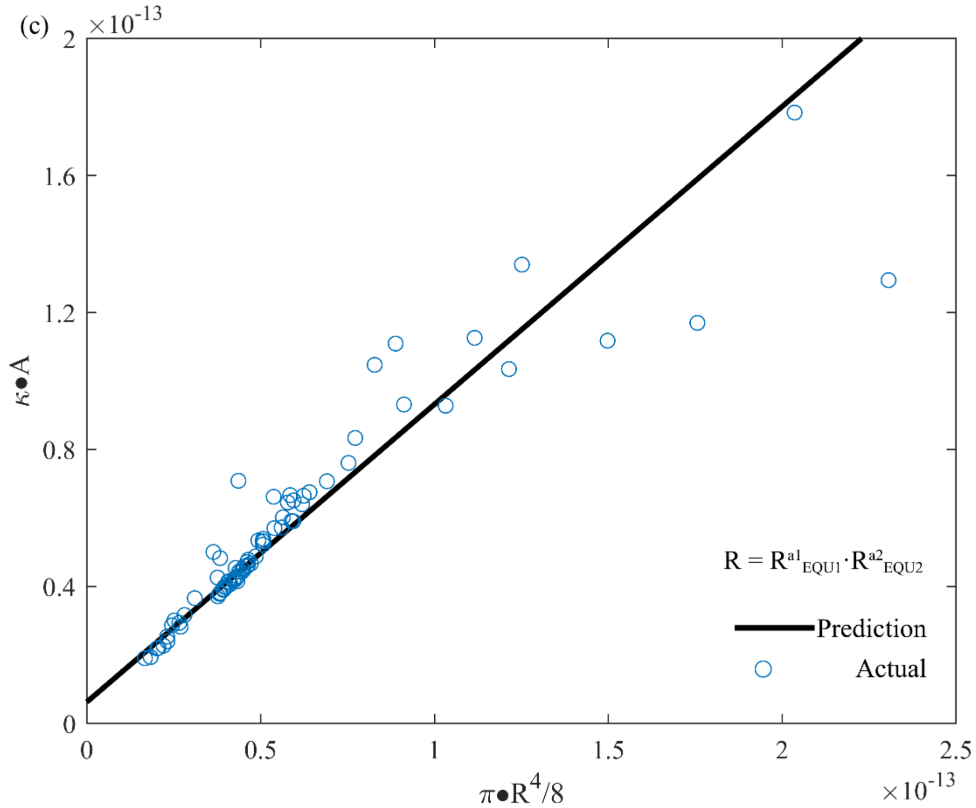

Fig. 9 Three best-performance characteristic radius formulations from the optimisation of

shape-conductivity relation using characteristic radius represented by: (a) $\sum_{i=1}^{3} a_i r_{\mathrm{EQU}i}$; (b) $\left(\sum_{i=1}^{3} a_i r_{\mathrm{EQU}i}^{4}\right)^{1/4}$; (c) $\prod_{i=1}^{3} r_{\mathrm{EQU}i}^{a_i}$.

Based on the analysis above, $0.5943 \cdot R_{\mathrm{EQU1}} + 0.4057 \cdot R_{\mathrm{EQU2}}$ is the optimal characteristic radius formulation for reconstruction of the varying-radius pipeline model. The first equivalent radius and the second equivalent radius computed directly from each slice of the binary fractures, and the optimal characteristic radius determined for all slices of the binary fractures from the first equivalent radius and the second equivalent radius are illustrated in Fig. 10. Two selected cross-sections from the RF experiment and the corresponding cross-sections from the RD experiment are presented in Fig. 10 a to demonstrate where the fracture ends up with increased cross-sectional area (second equivalent radius in Fig. 10 b) yet reduced inscribed radius (first equivalent radius in Fig. 10 a) after exposure. As it can be seen from Fig. 10 c, although the varying-radius pipeline model simplifies the shape of flow cross-sections, it preserves the resolution of the cross-sectional variation along the dominate flow path: The characteristic radius of the post-exposure fracture in RD experiment is smaller than the characteristic pre-exposure radius and shows a high frequency and low amplitude variation; the characteristic radius of the post-exposure fracture in RF experiment is generally larger and shows a low frequency and high amplitude variation.

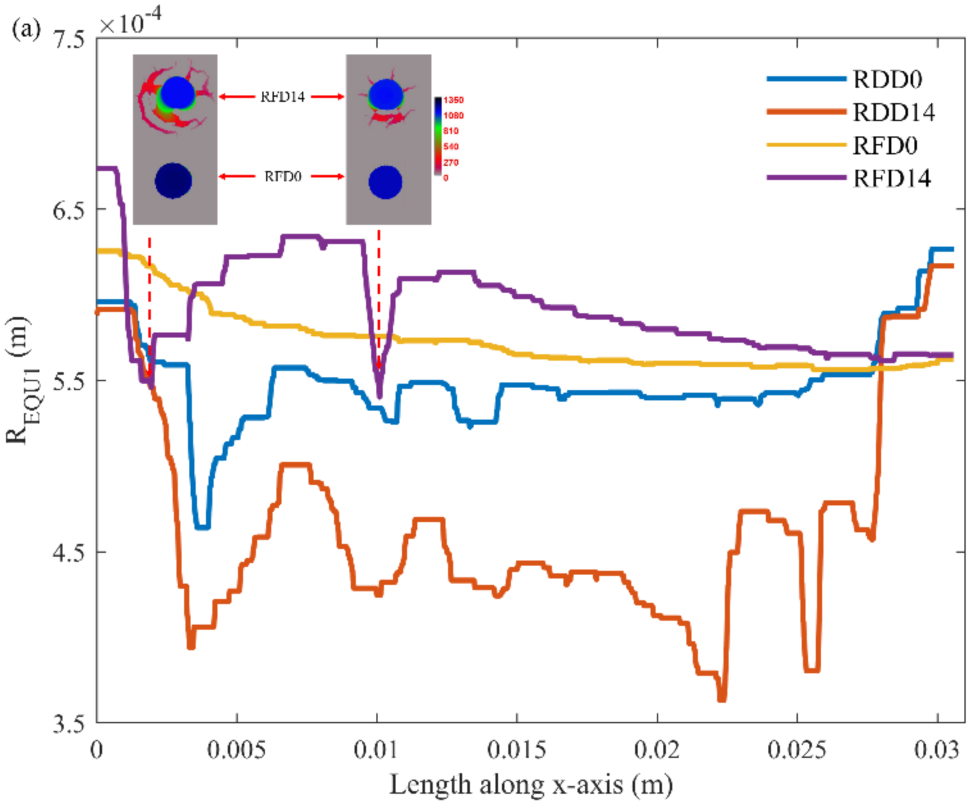
(a)
×10-4
RDD0
RDD14
RFD0
RFD14
RFD14
RFD0
1350
1080
810
540
270
0
R_EQU1 (m)
Length along x-axis (m)

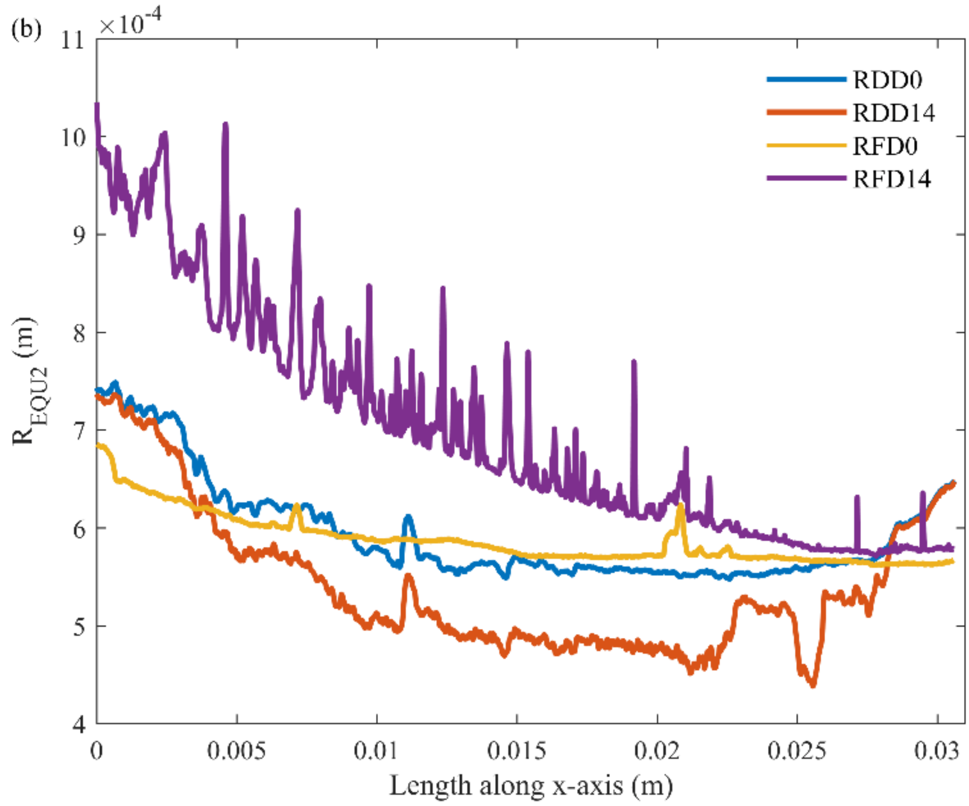
(b)
×10-4
RDD0
RDD14
RFD0
RFD14
R_EQU2 (m)
Length along x-axis (m)

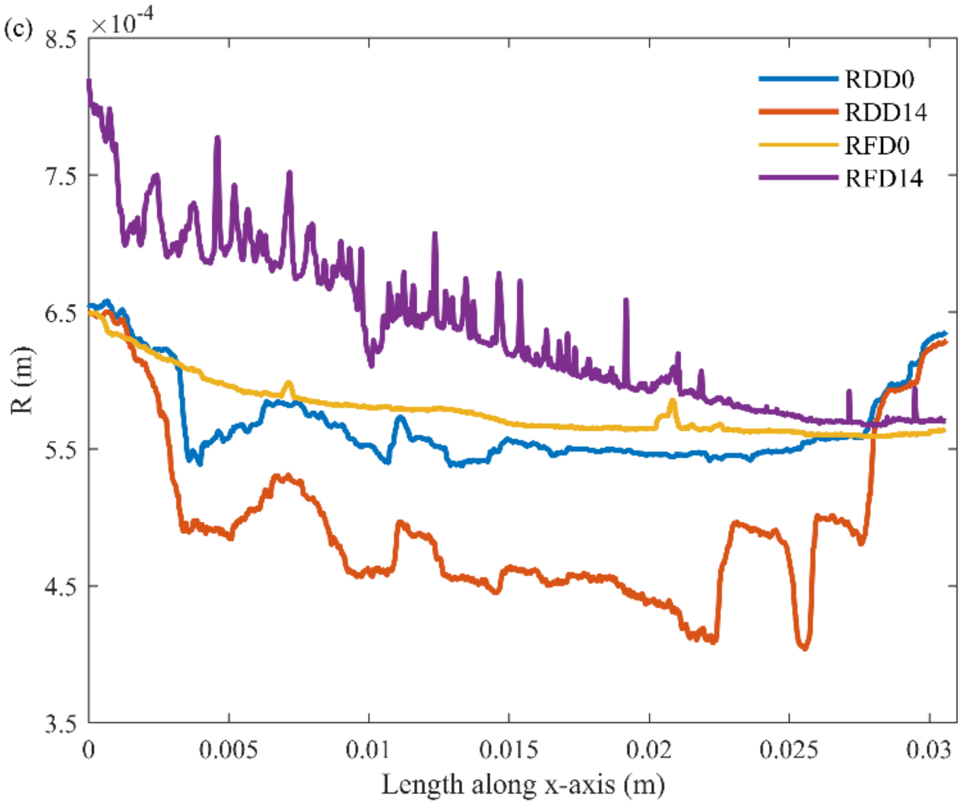

Fig. 10 Re-evaluation of characteristic radius directly from binary fractures using the optimal characteristic radius formulation: (a) first equivalent radius; (b) second equivalent radius; (c) characteristic radius ($R = 0.5943 \cdot R_{EQU1} + 0.4057 \cdot R_{EQU2}$).

4.4 Varying-radius pipeline modelling and permeability re-evaluation

One dimensional Navier-Stokes flow through a pipeline with varying characteristic radius was carried out to re-evaluate the hydraulic properties of the fractures. The numerical result revealing the change of the characteristic radius, velocity and pressure drop along the pipelines (fractures) is illustrated on Fig. 11.

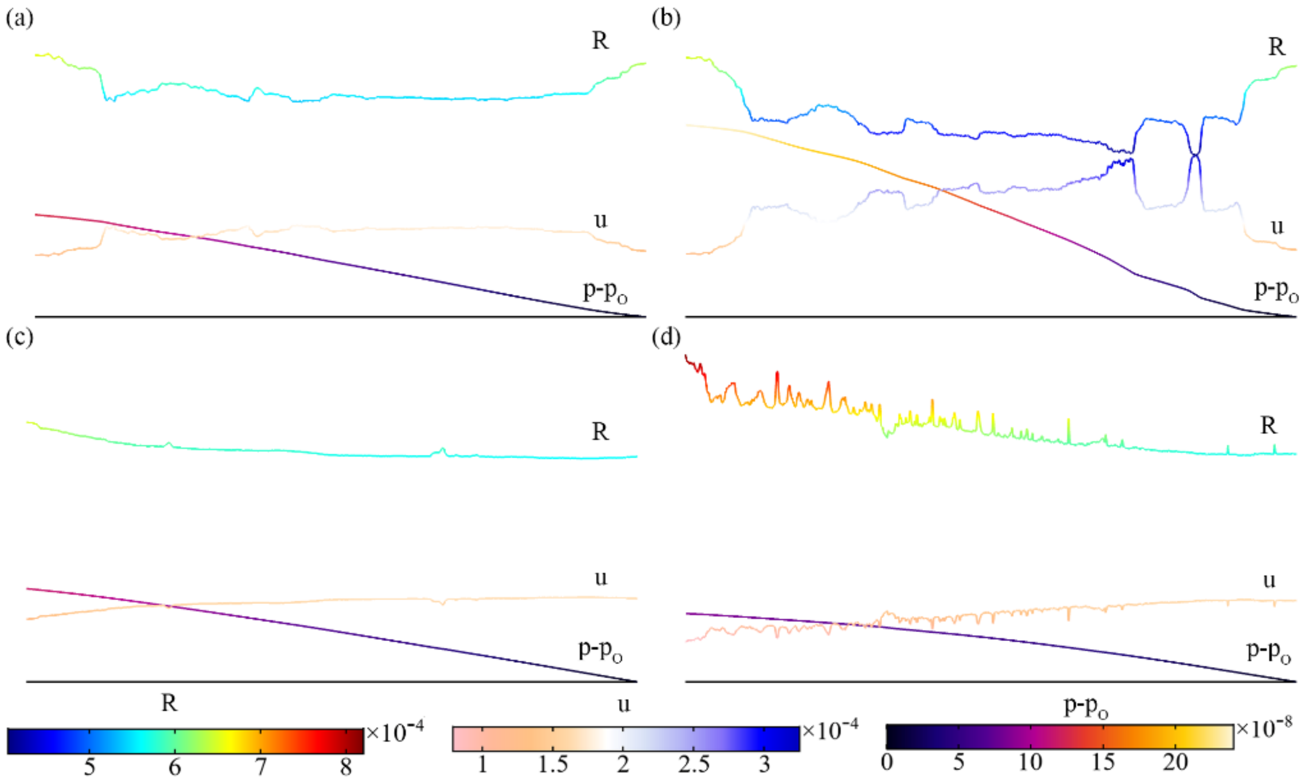

Fig. 11 Profiles of velocity and pressure drop obtained from varying-radius pipeline modelling for fractures: (a) RDD0; (b) RDD14; (c) RFD0; (d) RFD14.

Local and average permeability, as well as conductivity, solved from the varying-radius pipeline modelling is plotted on Fig. 12. As it is revealed from Fig. 12, the varying-radius pipeline model is capable of addressing the heterogeneity of hydraulic properties along the flow path. The average conductivity (or permeability) is again higher than the minimum of the cross-sectional conductivity (or permeability), the phenomenon is also observed in direct pore-scale modelling. This indicates that using conductivity of the smallest cross-section to represent a single fracture or a pore-throat in Pore Network Model or Pipe Network Model might not be plausible. The average permeability according to varying-radius pipeline modelling are 3.93×10^{-8} m^2, 2.73×10^{-8} m^2, 4.14×10^{-8} m^2 and 4.68×10^{-8} m^2 respectively for RDD0, RDD14, RFD0 and RFD14.

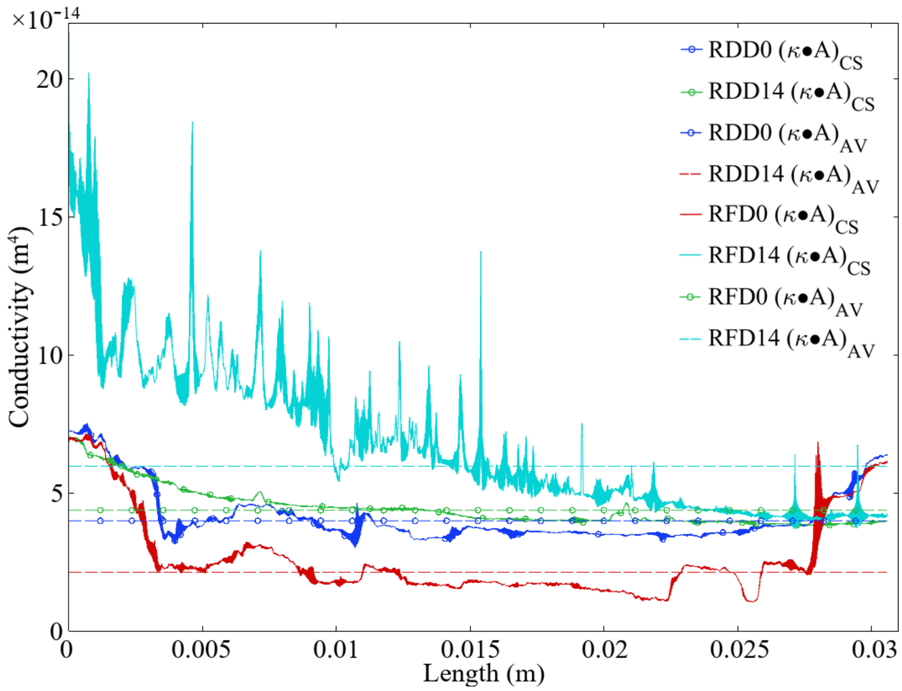

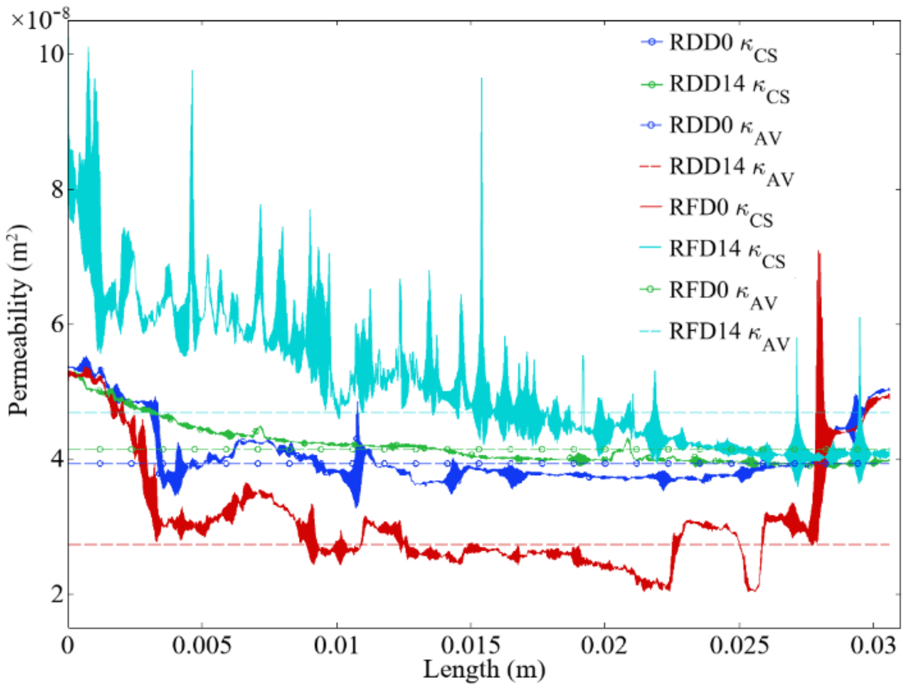

Fig. 12 Conductivity and permeability re-evaluated for the fractures from varying-radius pipeline modelling.

A comparison of the fracture permeability evaluated from permeability test, 3D direct pore-scale modelling and 1D varying-radius pipeline modelling is provided on Fig. 13. The ranges of relative error by simulation are -7.33%–4.05% for the direct pore-scale modelling and -7.77%–10.64% for the varying-radius pipeline modelling. As it can be seen, permeability predictions by the two simulation methods are close to permeability evaluated from the permeability test, and the prediction by direct pore-scale modelling is slightly better than the prediction by varying-radius pipeline modelling. However, the procedure for direct pore-scale modelling is more complicated, and more computationally demanding. The memory required for the direct pore-scale modelling was up to 70 GB and the CPU time was up to 40 cores × 30 min for a single fracture image (up to 17322892 unstructured mesh elements), while it took less than 40 cores × 10 sec CPU time to solve the varying-radius pipeline model in batch for all four fracture images (2000 mesh elements for each fracture) using about 1 GB memory.

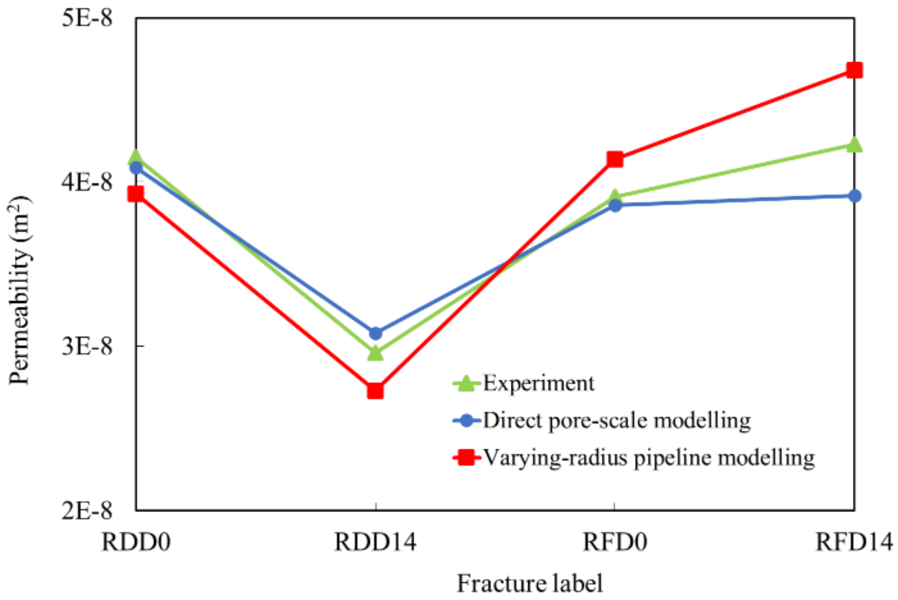

Fig. 13 Comparison of fracture permeability evaluated from different methods.

5. Conclusion

In this study, two types of aqueous CO_2–cement interaction experiments, a reactive-diffusion (RD) type of interaction and a reactive-flow (RF) type of interaction, were designed to investigate the different patterns of cement fracture morphological and aperture alterations as a result of aqueous CO_2 attack with the aid of X-ray imaging. A large amount of cement dissolution due to H^+ attack was observed on the surface of the fracture in the RF experiment, and notable precipitation of calcite on the surface of the fracture was unveiled in the RD experiment. Fracture patterns in the RF experiment after reaction with CO_2 showed distinguished layers of degradation, carbonation, and depletion. [stop] A large number of radial tensile micro-fractures and a small number of axial shear-tensile micro-fractures on the surface of the fracture were also observed. The fracture in the RD experiment after reaction showed a roughness increase.

Direct pore-scale modelling of Navier–Stokes flow through the fractures was carried out to estimate the average fracture permeability before and after interaction and to study the relation between the shape (i. e. area, perimeter and inscribed radius) and the permeability of fracture cross-sections. The optimal characteristic radius formulation as a generalised average of the three types of equivalent radius (determined by area, perimeter and inscribed radius) for the fractures was derived by searching a characteristic radius formulation that results in the minimal distance between the conductivity evaluated from Darcy's law ($\kappa \cdot A$) and the conductivity evaluated from Poiseuille's equation ($\pi R^4/8$). The formulation of the optimal characteristic radius ($0.5943 \cdot R_{EQU1} + 0.4057 \cdot R_{EQU2}$) suggests that the first equivalent radius (inscribed radius) and the second equivalent radius (sqrt(A/π)) have significant influence on the hydraulic conductivity.

Varying-radius pipeline model which is capable of addressing heterogeneous micro-structure alteration was reconstructed from the 3D binary image of fracture using the optimal characteristic radius formulation. Modelling of Navier–Stokes flow through the varying-radius pipe representation of fracture was proposed to re-evaluate the permeability. Comparison of numerically derived fracture permeability and the experimental result showed that the relative error by simulation are -7.33%–4.05% for direct pore-scale modelling and -7.77%–10.64% for varying-radius pipeline modelling.

While both methods are capable of estimating local permeability evolution at comparable accuracy, direct pore-scale modelling prevails in visualisation of local velocity field distribution, but requires complicated procedure of constructing realistic geometry and large computation capacity. Varying-radius pipeline modelling prevails in fast computation but requires establishment of accurate shape-permeability relation to construct a representative varying-radius pipe. Direct pore-scale modelling with coupled hydro-chemo-mechanical processes could be a promising method to investigate the micro-scale mechanisms of permeability evolution and the varying-radius pipeline modelling has the potential to assess large-scale CO_2 leakage.

Acknowledgment

This work is supported by the National Natural Science Foundation of China projects (41807275, 52074259, U1967208 and 41902258), and National key R&D program of China (2019YFE0100100).

References

[1] J.C. Chow, J.G. Watson, A. Herzog, S.M. Benson, G.M. Hidy, W.D. Gunter, S.J. Penkala, C.M. White, Separation and Capture of CO2 from Large Stationary Sources and Sequestration in Geological Formations, Journal of the Air & Waste Management Association, 53(10) (2003) 1172-1182.

[2] S. Bachu, M. Celia, Assessing the potential for CO_2 leakage, particularly through wells, from geological storage sites. Carbon Sequestration and Its Role in the Global Carbon Cycle, Geophysical Monograph Series, 183 (2009) 203-216.

[3] J.T. Adeoye, C. Beversluis, A. Murphy, V.C. Li, B.R. Ellis, Physical and chemical alterations in engineered cementitious composite under geologic CO2 storage conditions, International Journal of Greenhouse Gas Control, 83 (2019) 282 - 292.

[4] H.B. Jung, W. Um, Experimental study of potential wellbore cement carbonation by various phases of carbon dioxide during geologic carbon sequestration, Applied Geochemistry, 35 (2013) 161-172.

[5] E.B. Nelson, D. Guillot, Well Cementing, 2nd ed., Schlumberger, TX, USA, 2006.

[6] B.G. Kutchko, B.R. Strazisar, D.A. Dzombak, G.V. Lowry, T. Niels, Degradation of Well Cement by CO2 under Geologic Sequestration Conditions, Environmental science & technology, 41(13) (2007) 4787.

[7] J.P.L. Brunet, L. Li, Z.T. Karpyn, B.G. Kutchko, B. Strazisar, G. Bromhal, Dynamic Evolution of Cement Composition and Transport Properties under Conditions Relevant to Geological Carbon Sequestration, Energy & Fuels, 27(8) (2013) 4208-4220.

[8] L. Zhang, Y. Wang, X. Miao, M. Gan, X. Li, Geochemistry in geologic CO_2 utilization and storage: A brief review, Advances in Geo-Energy Research, 3(3) (2019) 304-313.

[9] S. Carroll, J.W. Carey, D. Dzombak, N.J. Huerta, L. Li, T. Richard, W. Um, S.D.C. Walsh, L. Zhang, Review: Role of chemistry, mechanics, and transport on well integrity in CO2 storage

environments, International Journal of Greenhouse Gas Control, 49 (2016) 149-160.
[10] S. Bachu, D.B. Bennion, Experimental assessment of brine and/or CO_2 leakage through well cements at reservoir conditions, International Journal of Greenhouse Gas Control, 3(4) (2009) 494-501.
[11] E. Liteanu, C.J. Spiers, C.J. Peach, E. Liteanu, C.J. Spiers, C.J. Peach, Failure behaviour wellbore cement in the presence of water and supercritical CO 2, Energy Procedia, 1(1) (2009) 3553-3560.
[12] M. Wigand, J.P. Kaszuba, J.W. Carey, W.K. Hollis, Geochemical effects of CO 2 sequestration on fractured wellbore cement at the cement/caprock interface, Chemical Geology, 265(1–2) (2009) 122-133.
[13] T. Yalcinkaya, M. Radonjic, C.S. Willson, S. Bachu, Experimental study on a single cement-fracture using CO 2 rich brine, Energy Procedia, 4 (2011) 5335-5342.
[14] P. Cao, Z.T. Karpyn, L. Li, Self-healing of cement fractures under dynamic flow of CO2-rich brine, Water Resources Research, 51(6) (2015) 4684-4701.
[15] E. Liteanu, C.J. Spiers, Fracture healing and transport properties of wellbore cement in the presence of supercritical CO2, Chemical Geology, 281(3) (2011) 195-210.
[16] X. Miao, L. Zhang, Y. Wang, L. Wang, X. Fu, M. Gan, X. Li, Characterisation of wellbore cement microstructure alteration under geologic carbon storage using X-ray computed micro-tomography: A framework for fast CT image registration and carbonate shell morphology quantification, Cement and Concrete Composites, 108 (2020) 103524.
[17] P. Cao, Z.T. Karpyn, L. Li, Dynamic alterations in wellbore cement integrity due to geochemical reactions in CO2-rich environments, Water Resources Research, 49(7) (2013) 4465-4475.
[18] S. Kabilan, H.B. Jung, A.P. Kuprat, A.N. Beck, T. Varga, C.A. Fernandez, W. Um, Numerical Simulation of Permeability Change in Wellbore Cement Fractures after Geomechanical Stress and Geochemical Reactions Using X-ray Computed Tomography Imaging, Environmental science & technology, 50(12) (2016) 6180-6188.
[19] X. Miao, K.M. Gerke, T.O. Sizonenko, A new way to parameterize hydraulic conductances of pore elements: A step towards creating pore-networks without pore shape simplifications, Advances in Water Resources, 105 (2017) 162–172.
[20] X. Miao, G.A. Narsilio, A. Wu, B. Yang, A 3D dual pore-system leaching model. Part 1: Study

on fluid flow, Hydrometallurgy, 167 (2017) 173–182.

[21] G.A. Narsilio, O. Buzzi, S. Fityus, T.S. Yun, D.W. Smith, Upscaling of Navier–Stokes equations in porous media: Theoretical, numerical and experimental approach, Comput Geotech, 36(7) (2009) 1200–1206.

[22] A.Q. Raeini, M.J. Blunt, B. Bijeljic, Direct simulations of two-phase flow on micro-CT images of porous media and upscaling of pore-scale forces, Advances in Water Resources, 74 (2014) 116–126.

[23] H.L. Ramandi, P. Mostaghimi, R.T. Armstrong, Digital rock analysis for accurate prediction of fractured media permeability, J Hydrol, 554 (2017) 817–826.

[24] D. Crandall, G. Bromhal, Z.T. Karpyn, Numerical simulations examining the relationship between wall-roughness and fluid flow in rock fractures, International Journal of Rock Mechanics and Mining Sciences, 47(5) (2010) 784-796.

[25] H. Deng, B.R. Ellis, C.A. Peters, J.P. Fitts, D. Crandall, G.S. Bromhal, Modifications of Carbonate Fracture Hydrodynamic Properties by CO2-Acidified Brine Flow, Energy & Fuels, 27(8) (2013) 4221-4231.

[26] M.J. Blunt, B. Bijeljic, H. Dong, O. Gharbi, S. Iglauer, P. Mostaghimi, A. Paluszny, C. Pentland, Pore-scale imaging and modelling, Advances in Water Resources, 51(1) (2013) 197–216.

[27] P. Maheshwari, R.R. Ratnakar, N. Kalia, V. Balakotaiah, 3-D simulation and analysis of reactive dissolution and wormhole formation in carbonate rocks, Chemical Engineering Science, 90 (2013) 258-274.

[28] J.P. Pereira Nunes, M.J. Blunt, B. Bijeljic, Pore-scale simulation of carbonate dissolution in micro-CT images, Journal of Geophysical Research: Solid Earth, 121(2) (2016) 558-576.

[29] M. Liu, P. Mostaghimi, High-resolution pore-scale simulation of dissolution in porous media, Chemical Engineering Science, 161 (2017) 360-369.

[30] S. Bakke, P.E. Oren, 3-D Pore-Scale Modelling of Sandstones and Flow Simulations in the Pore Networks, Spe Journal, 2(2) (1997) 136-149.

[31] T.W. Patzek, D.B. Silin, Shape Factor and Hydraulic Conductance in Noncircular Capillaries : I. One-Phase Creeping Flow, Journal of Colloid & Interface Science, 236(2) (2001) 295-304.

[32] S.J. Salter, K.K. Mohanty, Multiphase Flow in Porous Media: I. Macroscopic Observations and Modeling, in: SPE Annual Technical Conference and Exhibition, Society of Petroleum

Engineers, New Orleans, Louisiana, 1982, pp. 23.
[33] E. Aker, K. JØrgen MÅlØy, A. Hansen, G.G. Batrouni, A Two-Dimensional Network Simulator for Two-Phase Flow in Porous Media, Transport in Porous Media, 32(2) (1998) 163-186.
[34] L.W. Rong, K.J. Dong, A.B. Yu, Lattice-Boltzmann computation of hydraulic pore-to-pore conductance in packed beds of uniform spheres, Chemical Engineering Science, 224 (2020) 115798.
[35] S.L. Bryant, P.R. King, D.W. Mellor, Network model evaluation of permeability and spatial correlation in a real random sphere packing, Transport in Porous Media, 11(1) (1993) 53-70.
[36] P.H. Valvatne, M.J. Blunt, Predictive pore-scale modeling of two-phase flow in mixed wet media, Water Resources Research, 40(7) (2004) W07406.
[37] W. Xu, Y. Zhang, X. Li, X. Wang, P. Zhang, Study on three-dimensional fracture network connectivity path of rock mass and seepage characteristics based on equivalent pipe network, Environmental Earth Sciences, 78(16) (2019) 516.
[38] C. Xu, C. Fidelibus, P. Dowd, Realistic pipe models for flow modelling in Discrete Fracture Networks, in: 1st International Discrete Fracture Network Engineering Conference, Vancouver, Canada, 2014.
[39] P.-E. Oren, S. Bakke, O.J. Arntzen, Extending predictive capabilities to network models, SPE Journal, 3(04) (1998) 324-336.
[40] J.O. Helland, A.V. Ryazanov, M.I.J.v. Dijke, Characterization of Pore Shapes for Pore Network Models in: the 11th European Conference on the Mathematics of Oil Recovery (ECMOR XI), Bergen, Norway, 2008.
[41] S. Sisavath, X. Jing, R.W. Zimmerman, Creeping flow through a pipe of varying radius, Physics of Fluids, 13(10) (2001) 2762-2772.
[42] M. Hemmat, A. Borhan, Creeping flow through sinusoidally constricted capillaries, Physics of Fluids, 7(9) (1995) 2111-2121.
[43] Y.J. Jeong, K.S. Youm, T.S. Yun, Effect of nano-silica and curing conditions on the reaction rate of class G well cement exposed to geological CO2-sequestration conditions, Cement and Concrete Research, 109 (2018) 208-216.
[44] B.G. Kutchko, B.R. Strazisar, G.V. Lowry, D.A. Dzombak, N. Thaulow, Rate of CO2 attack on hydrated Class H well cement under geologic sequestration conditions, Environmental science

& technology, 42(16) (2008) 6237.

[45] D. Tiab, E.C. Donaldson, Chapter 8 - Naturally Fractured Reservoirs, in: D. Tiab, E.C. Donaldson (Eds.) Petrophysics (Second Edition), Gulf Professional Publishing, Burlington, 2004, pp. 488-553.

[46] D. Tiab, E.C. Donaldson, Chapter 3 - Porosity and Permeability, in: D. Tiab, E.C. Donaldson (Eds.) Petrophysics (Fourth Edition), Gulf Professional Publishing, Boston, 2016, pp. 67-186.

[47] J. Schindelin, I. Arganda-Carreras, E. Frise, V. Kaynig, M. Longair, T. Pietzsch, S. Preibisch, C. Rueden, S. Saalfeld, B. Schmid, J.-Y. Tinevez, D.J. White, V. Hartenstein, K. Eliceiri, P. Tomancak, A. Cardona, Fiji: an open-source platform for biological-image analysis, Nature Methods, 9 (2012) 676.

[48] P. Cignoni, M. Callieri, M. Corsini, M. Dellepiane, F. Ganovelli, G. Ranzuglia, MeshLab: an Open-Source Mesh Processing Tool, in: V. Scarano, R.D. Chiara, U. Erra (Eds.) Eurographics Italian Chapter Conference, Eurographics Association, 2008, pp. 129-136.